An-Najah National University
Faculty of Graduate Studies

EFFECT OF THE BEAM EMITTANCE ON THE PHOTON FLUX AND BRIGHTNESS OF SYNCHROTRON RADIATION EMITTED BY THE UNDULATOR U20

By
Thiab Abdalhakim Diyab Dubeik

Supervisors
Dr. Hadil Abualrob
Prof. Sameer Ikhdair

This Thesis is Submitted in Partial Fulfillment of the Requirements for the Degree of Master of Physics, Faculty of Graduate Studies, An-Najah National University, Nablus - Palestine.

2026

EFFECT OF THE BEAM EMITTANCE ON THE PHOTON FLUX AND BRIGHTNESS OF SYNCHROTRON RADIATION EMITTED BY THE UNDULATOR U20

By
Thiab Abdalhakim Diyab Dubeik

This Thesis was defended successfully on 16/02/2026 and approved by:

Dr. Hadil Abualrob	
Supervisor	Signature
Prof. Sameer Ikhdair	
Co-Supervisor	Signature
Dr. Wafaa Khater	
External Examiner	Signature
Prof. Mohammad Abu Jaafar	
Internal Examiner	Signature

Dedication

To my mother and father, the source of my strength and determination.

To my wife, whose presence, understanding, and constant support carried me through every challenge of this journey.

To my family, with all my gratitude and love—this work is dedicated to you.

And to the soul of my dear friend, Omar Kaabi always in my heart, never forgotten.

Acknowledgment

I want to express my deepest gratitude to my supervisors, Dr. Hadil Abualrob and Prof. Dr. Sameer Ikhdair, for their continuous guidance, encouragement, and invaluable support throughout this work. Their scientific patience has played a major role in shaping this thesis.

I am also grateful to the Department of Physics at An-Najah National University for their academic and administrative support and for providing the environment that made this work possible, particularly Dr. Ahmed Bassalat, for the great effort he made to ensure the success of this thesis.

Finally, I would like to express my heartfelt gratitude to my family and friends for their continuous encouragement, patience, and belief in me throughout this journey. To my mother and father, my wife, my sisters, and my brothers, your support has been the foundation of this achievement, and without it, this milestone would not have been possible.

Declaration

I, the undersigned, declare that I submitted the thesis entitled:

EFFECT OF THE BEAM EMITTANCE ON THE PHOTON FLUX AND BRIGHTNESS OF SYNCHROTRON RADIATION EMITTED BY THE UNDULATOR U20

I declare that the work provided in this thesis, unless otherwise referenced, is the researcher's own work, and has not been submitted elsewhere for any other degree or qualification.

Student's Name	**Thiab Abdalhakim Diyab Dubeik**
Signature:	
Date:	**29/11/2023**

List of Contents

List of Tables

List of Figures

List of Appendices

EFFECT OF THE BEAM EMITTANCE ON THE PHOTON FLUX AND BRIGHTNESS OF SYNCHROTRON RADIATION EMITTED BY THE UNDULATOR U20

By
Thiab Abdalhakim Diyab Dubeik
Supervisors
Dr. Hadil Abualrob
Prof. Sameer Ikhdair

Abstract

This thesis investigates the radiation performance of the U20 undulator for a potential future installation at SESAME, and the magnetic design of the sector dipole for the PERLE. The study aims to evaluate how beam parameters affect photon flux and brightness, and to provide a validated magnetic model for PERLE. Using SRW simulations, the U20 undulator was analyzed under realistic SESAME beam conditions, showing that reducing the horizontal emittance significantly enhances light output: the fundamental harmonic increased from 2.46×10^{13} to 3.28×10^{13} while the brightness improved by nearly an order of magnitude. These performance gains can be directly adopted by SESAME in future upgrades.

In the second part, the PERLE dipole magnet was designed and optimized using Opera 3D, achieving uniform field quality across the Good Field Region and confirming an efficient turbulent water-cooling regime (Re = 9685). The resulting magnetic model forms part of the PERLE Technical Design Report (TDR). Overall, the outcomes of this work contribute to improving undulator performance at SESAME and advancing magnet development for PERLE.

Keywords: Undulator radiation, photon flux, brightness, dipole magnet, synchrotron radiation, Energy Recovery LINAC.

Chapter One

Introduction

Accelerators are machines that are used to accelerate charged particles at high speeds near to the speed of light [1]. Electric field is used to accelerate the charged particles and magnetic field is used to guide them along a curved path. Accelerators are widely used in fundamental research either as colliders or synchrotron light sources for applications in medicine, chemistry, biology, material science, nuclear science and many others.

Accelerators are classified as linear or circular. In a linear accelerator, the beam travels along a straight path and is dumped after each pass, reaching an energy level equivalent to the injection energy. This produces a high average current with constant beam power. In a circular accelerator, the beam undergoes numerous turns in a circular path without being dumped. To compensate for energy loss, energy is continuously injected into the beam. Linear and circular accelerators each have distinct advantages and disadvantages. Linear accelerators are simpler in design, as they accelerate particles along a straight path, avoiding the need for complex magnetic systems. They also avoid energy loss from synchrotron radiation, making them more efficient in certain applications, where high precision is crucial. However, linear accelerators require long structures to achieve high energies, making them space-consuming and costly. Circular accelerators, on the other hand, allow particles to complete multiple turns in a compact space, achieving very high energies. They can also produce high-intensity beams, which are beneficial for applications. However, circular accelerators suffer from energy loss due to synchrotron radiation, especially at higher energies, requiring continuous energy injection to maintain the beam's power. They also have a more complex design and higher maintenance costs due to the magnetic systems needed to maintain the beam's circular path. The Energy Recovery Linac (ERL) is another type of accelerator that combines the benefits of both linear and circular accelerators. It operates by recovering the energy from accelerated particles and using it to accelerate new bunches of electrons, which reduces power consumption and provides a more environment friendly beam dump. Similar to a linear accelerator, the ERL accelerates particles along a straight path, eliminating the need for complex bending magnets and offering high precision while avoiding energy loss from synchrotron radiation, a common issue in circular accelerators. Additionally, the ERL incorporates a circular design by recycling the beam's energy through a return loop, where

the energy is recovered before being dumped. This process helps to optimize power efficiency while maintaining high beam intensity, making the ERL a unique and efficient solution for high energy particle acceleration.

1.1 Circular accelerators

Circular accelerators have a wide range of applications in different fields [2], such as colliders, free electron lasers and synchrotron light sources.

A synchrotron is a circular accelerator that accelerates the charged particle usually electrons to travel in a curved trajectory under the influence of a magnetic field at a speed close to the speed of light and radiate electromagnetic radiation at each bend. This electromagnetic radiation is called synchrotron radiation [3]. Figure (A.1a) (see appendix A) shows a schematic view of the synchrotron. It consists of an electron gun as a source of electrons, linear accelerator (LINAC) that accelerates electrons to a few hundreds of MeV, a booster ring to boost the electron energy to few GeV, a storage ring that keeps the electrons circulating in closed orbit in the ring and the beamline that extracts out the synchrotron radiation for different applications such as medicine, chemistry and biology [4]. The storage ring, as in figure (A.1b) (see appendix A), consists of series of magnets with different types: bending magnets to bend the trajectory of the electron beam, quadrupoles to focus the electron beam in one plane and defocus in the other plane to prevent the increase in beam size, and sixtupoles to correct chromatic aberration when the electron energy is shifted from the nominal energy. Radio- frequency cavity generates electric field that accelerates the electrons to compensate for the energy loss due to synchrotron radiation at each bend in order to keep constant energy of the electrons. The arrival of the electron in the RF cavity is synchronized with the peak of the RF wave. Consequently, the electrons are grouped in bunches with ~10^{10} electron/bunch. Insertion devices (ID) including wigglers and undulators are essential elements in third generation light sources can be inserted in the straight sections between two bending magnets. An ID consists of a series of magnets in opposite polarities. It is used to generate high flux, high brightness synchrotron radiation.

Photon beam flux and brightness are important parameters for experiments using synchrotron radiation. Photon flux is defined as number of photons per unit time (photon/s) and brightness is defined as photon flux (photon /s) per unit source size per

unit solid angle (the angular divergence). The source size times the angular divergence is called the emittance (usually measured in nm.rad). To achieve high brightness, it is necessary to produce high flux photon beam and to keep low emittance electron beam. Modern synchrotrons are currently concentrating efforts on generating high flux radiation from short period undulators and are conducting total upgrades to achieve lower electron beam emittance. However, an upgrade project requires a big budget, total replacement of the available infrastructure and man power. Therefore, the first step towards lower emittance project for any synchrotron is to study the brightness and flux of synchrotron radiation emitted by the planned insertion devices before proceeding in a high cost upgrade and diving in fabrication of insertion devices.

This first part of this thesis considers calculating the photon flux and brightness of the undulator U20 (short period undulator) for future installation at SESAME synchrotron considering the current emittance and potential future lower emittance.

SESAME (Synchrotron Light for Experimental Science and Applications in the Middle East), is the unique synchrotron in the Middle East. It is located in Jordan. Developed under UNESCO's auspices, SESAME is a cooperative project involving scientists and governments from the region, modeled after CERN. Palestine is one of the member countries of this international project.

Recently, synchrotron light sources have shown important achievements in reducing the emittance to pm.rad. However, the emittance of SESAME (26 nm.rad) is still high compared to other synchrotrons. Table 1 shows the state of the out of low emittance synchrotron light sources in the world towards lower emittance (in the order of pm.rad) to reply to the growing scientific demand in different fields. However, SESAME is still operating at a relatively high emittance. Hence, it is important to start a study of the spectral performance of some undulators to be installed after a lower emittance upgrade project.

Table 1

Low-emittance for some of the synchrotrons in the world

Name of synchrotron and its place	Energy of beam (GeV)	Value of emittance
SESAME (Jordan) [7]	2.5	26 nm rad
ALS (US)	1.9	2 nm rad
ALS-U (US) [8]	2	70 pm rad
DIAMOND(US) [9]	3	150 nm rad
DIAMOND- II (US) [10]	3.5	160 pm rad
ESRF (France) [11] [12]	6	4 nm rad
ESRF-EBS (France) [12]	6	134 pm rad
SOLEIL (France) [13]	2.75	4 nm rad
SOLEIL- II (France) [13]	2.75	84 pm rad
NSLS-II (US) [14]	3	2.1 nm
NSLS-II CB(US) [14]	3	0.065 nm
Spring-8 (Japan) [15]	8	3500 pm rad
Spring-8 II (Japan) [15]	6	67 pm rad

1.2 Energy Recovery LINAC (ERL)

The ERL principle is based on recovering the energy from the accelerated beam when it passes through a decelerating section which uses its kinetic energy to accelerate new bunches of electrons leading to significant energy saving. First proposed in 1965 by Maury Tigner [16].

Figure A.2 (see appendix A) shows the state of the all of ERL in the world. Three Energy Recovery Linac (ERL) facilities are completed and shown in orange on the diagram, such as ALICE in Daresbury- Europe [17], the first European ERL with modest current and energy, which closed after ten successful years; CEBAF [18], which achieved the highest single-pass energy of 1 GeV; and JLab FEL [19], which reached the highest current of 10 mA among SRF ERLs. Six ERLs are ongoing, marked in green and dark green, including both cold and warm systems, such as S-DALINAC [20] at Darmstadt University in Germany, a superconducting linear accelerator; CBETA [21] at Cornell University, at US, the first multi-pass SRF accelerator with similar energy to S-DALINAC but higher current; and MESA ERL at Mainz [22], expected to be significant with 100 MeV of energy, and set for its first test in 2025.

Four ERLs are in progress, depicted in dark blue: CEBAF ERL at Jefferson Lab [18], designed to achieve about 104 MeV over five passes, PERLE in Orsay, France, aims for a current of 20 mA and energy of 500 MeV. This facility is a step towards future ERLs like the LH_eC [23], which targets 50 GeV.

PERLE (Powerful Energy Recovery LINAC for Experiments) is an international collaboration between different scientific research centers and universities from France, the UK, Spain, Switzerland, the USA and An-Najah National University as the partner from the middle east region.

PERLE is designed to demonstrate the practical applications of ERL technology, known as energy efficiency from recovery of energy and reusing this energy to accelerate new bunches of electrons. This feature of PERLE enables it to be used more widely for this technology in a larger system such as a large hadron electron collider (LH_eC), proposed in the future with a maximum energy of 50GeV. PERLE is a prototype and a test for the LHeC for ERL due to their identical parameters [24], which contributes to developing the ERL technology for high energy physics. PERLE will also be a facility for scientific applications such as nuclear study.

Figure A.3 (see appendix A) illustrates the top view footprint of the PERLE accelerator operating at 500 MeV. In this system, electrons are first injected into the LINAC (Linear Accelerator) section, where they are accelerated using radiofrequency (RF) cavities to reach the desired final energy. After the electrons achieve this high energy, the beam is directed back into the RF cavity, but with a 180º phase shift. This phase shift causes the beam to decelerate, reducing its energy back to the initial injection energy. Importantly, the energy lost during this deceleration process is not wasted. Instead, it is transferred to accelerate a new bunch of electrons, a key feature of the Energy Recovery LINAC (ERL) technology. Dipoles are used to bend the trajectory of the electron beam and quadrupoles are used focus/defocus the beam.

The second part of this thesis considers performing a complete magnetic design for one family of the dipoles of PERLE called the S-Bend, which is the first step before launching the fabrication process. Later the fabricated magnets will measure and characterized to cross-check the measurements with the data obtained in this work.

In summary, the work of thesis is organized as follows:

1. Studying the spectral performance of synchrotron radiation emitted by the U20 undulator, with an emphasis on the impact of reducing emittance and energy spread on the flux and brightness of synchrotron radiation, particularly in the context of its future installation at SESAME. Calculations are carried out with SRW simulation code available with the accelerator physics group at An-Najah University.
2. Carrying out magnetic design of the S-Bend dipoles for the PERLE accelerator. Magnetic design is carried out with OPERA 3D software. This part was carried out at the IJClab in Paris-Saclay University during a two-month stay in the summer of 2023.

Chapter Two

Magnets for particle accelerators

According to the theory of electromagnetism, when relativistic charged particle passes through a magnetic field perpendicular to its direction of motion, its trajectory is bent and part of its energy is lost in the form of synchrotron radiation. In accelerators, the most common simple field used to bend the trajectory of accelerated charged particles is a constant field generated by dipole magnet. In general, dipole magnets are essential components in any circular accelerator.

Insertion devices are other magnetic devices used in accelerators. They are basically used in synchrotron light sources for producing high flux, high brightness synchrotron radiation.

2.1 Technology of accelerator magnets

There are many technologies used in accelerator magnets to produce the magnetic field. Permanent magnets [25], it is fabricated by placing a conductor in an external magnetic field, and when the field is removed, it keeps its magnetization. Superconducting magnets [26] are used for high-energy accelerators that require a magnetic field (> 2T) as the Large Hadron Collider LHC. Electromagnetic technology is used to generate a magnetic field through a current-carrying conductor.

This thesis considers electromagnet technology for the dipoles of PERLE and permanent magnet technology for the undulator U20 for SESAME.

2.2 Dipole magnets

The electromagnetic dipole consists mainly of two parts: a yoke and a coil.

The yoke, which forms the body of the dipole, is usually made of massive iron or low-carbon steel due to its high magnetic permeability, allowing it to guide the magnetic flux efficiently.

The coil, which is wound around the poles with N turns, carries the electric current that generates the magnetic field. It is commonly fabricated from copper or aluminum because of their high electrical conductivity and relatively low resistive losses.

2.2.1 Coordinate system

For the description of the dipole magnetic field and the corresponding beam dynamics, a right-handed coordinate system is adopted, as illustrated in figure A.4 (see appendix A). According to the right-hand rule, the magnetic field is oriented along the negative *y*-axis. Consequently, for a negatively charged particle traveling in the negative *z*-direction, the resulting magnetic force is directed along the positive *x*-axis.

2.2.2 Types of dipole magnets

There are many types of electromagnetic dipoles: C-shaped, mainly used in synchrotrons with less mechanical stability, O-shape magnet of more mechanical stability but it has a zero-pole high [27]. An H-shaped magnet is similar to O-shaped in mechanical stability with symmetrical shape and symmetrical field distribution in the gap. Figure A.5 (see appendix A) shows the three main dipole geometries.

An H-shaped magnet and configuration of the magnetic field is shown in Figure A.6 (see appendix A).

2.2.3 Dipole pole shape

Scalar and vector potentials are used to describe how a field is distributed and the shape of the poles for a specific multipole order n. Equipotential are lines or surfaces where the value of either the scalar or vector potential remains the same. Vector equipotential represent the lines along which the field flux occurs for a multipole of order n. These lines show the direction of the field's influence. Scalar equipotential are lines that are perpendicular to the vector equipotential. They help define the shape of the poles that are needed to create a perfectly uniform multipole field.

The vector and scalar equipotential in $x - y$ plane are:

$$C_n(x + iy)^n = A(x, y) + iV(x, y) \quad \text{with} \quad z = x + iy \quad \ldots\ldots\ldots\ldots\ldots\ldots (1)$$

Where V is the magnetic scalar potential with $\vec{H} = -\vec{\nabla}V,\ A = A_z$

So, $A = A(x, y)\hat{z}$ and $B = \nabla x(A\hat{z})$

With field line $A = constant$ and C_n is a complex constant that sets the strength and phase of the n-pole, without loss of generality, taking C_n real in what follows, where n=1,

for the dipole magnet:

$$C_1(x + iy) = A + iV \quad \ldots\ldots\ldots\ldots\ldots\ldots \quad (2)$$

$A = C_1 x$ vector equipotential, $V = c_1 y$ scalar equipotential

Hence equipotential V = const are horizontal lines and streamlines A= const are vertical lines, producing a uniform field in the gap.

$A = V$, $C_1 x = c_1 y$

With high-permeability iron the pole faces coincide with scalar equipotential:

$$V = \pm V_0$$

The ideal dipole field generated at a scalar equipotential line. Gap h between poles for a dipole as shown in Figure A.7 (see appendix A), and the equation describing the pole shape:

$$y = \pm \frac{V_0}{c_1} = \pm \frac{h}{2} \quad \ldots\ldots\ldots\ldots\ldots\ldots \quad (3)$$

2.2.4 Dipole magnet field

According to Ampere's law, when current I flows in a coil of unit length dl and element of area da, the closed integral of the magnetic field B, stockes' theorem is given by:

$$\oint B.dl = \int \vec{\nabla} \times \vec{B} \cdot \overrightarrow{da} = \mu_0 I \quad \ldots\ldots\ldots\ldots\ldots\ldots \quad (4)$$

where μ_0 is the magnetic permeability of free space, dl is the length closed loop of the coil, and da is the area of the coil on a surface.

$$\left(\vec{\nabla} \times \vec{B}\right) \int \overrightarrow{da} = \mu_0 I \quad \ldots\ldots\ldots\ldots\ldots\ldots \quad (5)$$

$$\vec{\nabla} \times \vec{B} = \mu_0 \frac{I}{A} \quad \ldots\ldots\ldots\ldots\ldots\ldots \quad (6)$$

According to Maxwell's equation, the curl of the B-field is:

$$\vec{\nabla} \times \vec{B} = \mu_0 j \quad \ldots\ldots\ldots\ldots\ldots\ldots \quad (7)$$

Where $j = \frac{I}{A_{Coil}}$ is the current density, A is the area of the coil, and N is number of turns.

The integration of B for a closed path in a dipole magnet with gap h is consists of two parts: magnetic field in the gap, and magnetic field inside the yoke as shown in Figure A.8 (see appendix A).

$$\oint \frac{B}{\mu_O} \cdot dl = \oint_{Gap} \frac{B}{\mu_O} \cdot dl + \oint_{Yoke} \frac{B}{\mu_{steel}} \cdot dl = NI_{Dipole} \quad \ldots\ldots\ldots\ldots\ldots\ldots \quad (8)$$

Because the permeability of the steel μ_{steel} is very large compared to that in air, the second term of the equation (8) can be neglected. Therefore, it is inferred for a dipole magnet by Ampere turn relation:

$$NI_{Dipole} = \frac{B.h}{\mu_0} \quad \ldots\ldots\ldots\ldots\ldots\ldots \quad (9)$$

2.3 Insertion Devices

Insertion devices are specialized magnetic components placed in the trajectory of an electron beam within a synchrotron or storage ring. These devices create a periodic magnetic field that forces the electrons to follow a curved path, resulting in oscillations that produce synchrotron radiation. Their primary function is to enhance the emitted radiation's intensity and to regulate its wavelength by influencing the electron's motion through these periodic magnetic fields [28] [29].

Insertion devices consist of a sequence of magnets with alternating polarities that generate a periodic B-field, forcing the electrons to follow a sinusoidal path. There are two main types of insertion devices: wigglers and undulators. At each oscillation, electrons emit electromagnetic radiation, known as synchrotron radiation, at specific wavelengths. Wigglers generate strong magnetic fields that cause large angular deviations of the electron beam, resulting in a broad radiation spectrum. Conversely, undulators provide weaker but highly periodic magnetic fields, which lead to constructive interference of the emitted radiation and produce a narrow-band spectrum.

One of the most important advances in the development of insertion devices is the application of the Halbach magnet configuration. This arrangement of permanent magnets strengthens the magnetic field along the path of the electron beam while

suppressing it on the opposite side. Such a layout produces a highly uniform and nearly sinusoidal magnetic field. In undulators based purely on permanent magnets, Halbach arrays alone provide the required periodic field. However, in hybrid configurations, these arrays are combined with ferromagnetic components to boost the field amplitude and allow greater flexibility in tuning the device. Owing to these features, Halbach-based designs have become a cornerstone for achieving efficient, compact, and spectrally precise undulators and wigglers in modern synchrotron facilities [30].

The schematic illustration 2.6 (see appendix) shows the principle of a Halbach-based insertion device such as an undulator or a wiggler. The upper and lower rows represent arrays of permanent magnets arranged according to the Halbach configuration, where the magnetization direction of each block is rotated relative to its neighbors. This arrangement concentrates the magnetic field in the central gap, while reducing it on the outer sides. The green sinusoidal line indicates the trajectory of the electron beam, which oscillates periodically under the influence of the alternating magnetic field. The blue arrows represent the magnetic flux lines, demonstrating how the field is focused in the beam path. This configuration allows electrons to undergo controlled oscillations, thereby emitting synchrotron radiation with well-defined spectral properties.

2.3.1 The Equation of Motion Through Insertion Devices (ID)

Figure A.9 (see appendix A) shows a schematic view of ID of period λ_u.

When electrons propagate through insertion device, they are affected by the alternating magnetic field which is perpendicular to the direction of motion that causes the electrons to move in a sinusoidal trajectory as shown in Figure A.10 (see appendix A). At each bend, the accelerated electrons radiate synchrotron radiation as a cone with an emission angle of $1/\gamma$ (γ: $Lorentzfactor$. The radiation from different periods interfere constructively to generate high flux as shown in figure A.11 (see appendix A).

The coordinate usually used in synchrotrons is curvilinear coordinate system as shown in figure A.12 (see appendix A).

Considering vertical field undulator which is of a sinusoidal form:

$$B_z = B_0 sin(k_u s) \quad \ldots\ldots\ldots\ldots\ldots\ldots \quad (10)$$

where B_0 is the field amplitude and k_u is the wave number which is given by $k_u = \frac{2\pi}{\lambda_u}$

Inside the undulator, the Lorentz force acting on the electrons is:

$$\vec{F} = \vec{p} = \gamma m \vec{v} = e\left(\vec{E} + \vec{v} \times \vec{B}\right) \quad \ldots\ldots\ldots\ldots\ldots\ldots \quad (11)$$

where $\gamma = \frac{1}{\sqrt{1-\frac{v^2}{c^2}}}$ is the Lorentz factor, e is the electron charge, m is the mass of the electron, v is the velocity of the electron, E is the electric field and B is the magnetic field. The vertical motion of the electron in z- direction is neglected since it only moves in the horizontal x-z plane. The magnetic field and the velocity of the electron in undulator can then be written as

$$v = \begin{pmatrix} v_x \\ 0 \\ v_s \end{pmatrix}$$

$$B = \begin{pmatrix} 0 \\ B_z \\ B_s \end{pmatrix} \quad \ldots\ldots\ldots\ldots\ldots\ldots \quad (12)$$

After substituting Eq. (12) into Eq. (11) it provides:

$$m\gamma\dot{\vec{v}} = e\vec{v} \times \vec{B}$$

$$e\begin{pmatrix} v_x \\ 0 \\ v_s \end{pmatrix} \times \begin{pmatrix} 0 \\ B_z \\ B_s \end{pmatrix}$$

$$\dot{v} = \frac{e}{m\gamma}\begin{pmatrix} -v_s & B_z \\ -v_x & B_s \\ v_x & B_z \end{pmatrix} \quad \ldots\ldots\ldots\ldots\ldots\ldots \quad (13)$$

The last equation represents the acceleration of the electron in the undulator. Therefore, the acceleration in the x and s directions:

$$\ddot{x} = \frac{-e}{m\gamma}\dot{s}B_z(s) \quad \ldots\ldots\ldots\ldots\ldots\ldots \quad (14)$$

$$\ddot{s} = \frac{e}{m\gamma}\dot{x}B_z(s) \quad \ldots\ldots\ldots\ldots\ldots\ldots \quad (15)$$

Here the velocity in the x- direction $\dot{x}$ is very small with respect to the velocity in s-direction $\dot{s}$. So, longitudinal velocity: $\dot{s} = \beta c$ with $\beta = \frac{v}{C}$ is the relativistic velocity. Hence, Eq.14 becomes:

$$\ddot{x} = \frac{-e}{m\gamma}\dot{s}B_z(s) = \frac{-e}{m\gamma}\beta c B_0 sin(k_u s) \quad \ldots\ldots\ldots\ldots\ldots\ldots \quad (16)$$

It is more practical to express eq. 16 as a function of positions [31], by using the following transformation relations:

$\dot{x} = x'\beta c$

$\ddot{x} = x''\beta^2 c^2$

where, $x' = dx/ds$ and $x'' = d\,x'/ds$.

Therefore, Eq. 16 becomes

$$\ddot{x} = \frac{-e}{m\gamma}\beta c B_0 sin(k_u s)$$

$$x''\beta^2 c^2 = \frac{-e}{m\gamma}\beta c B_0 sin(k_u s)$$

$$x'' = \frac{-eB_0}{\beta m\gamma c} sin(k_u s) \quad \ldots\ldots\ldots\ldots\ldots\ldots \quad (17)$$

By integrating eq.17, one can obtain x' and x, as:

$$x' = \frac{eB_0}{K_u \beta m\gamma C} cos(k_u s) \quad \ldots\ldots\ldots\ldots\ldots\ldots \quad (18)$$

$$x = \frac{eB_0}{k_u^2 \beta m\gamma C} sin(k_u s) \quad \ldots\ldots\ldots\ldots\ldots\ldots \quad (19)$$

Further, substituting the value of $k_u = \frac{2\pi}{\lambda_u}$, Eqs. 18 and 19 becomes:

$$x' = \frac{eB_0\lambda_u}{2\pi\beta m\gamma c} cos\left(\frac{2\pi}{\lambda_u}s\right) \quad \ldots\ldots\ldots\ldots\ldots\ldots \quad (20)$$

$$x = \frac{eB_0\lambda_u^2}{4\pi^2\beta m\gamma c} sin\left(\frac{2\pi}{\lambda_u}s\right) \quad \ldots\ldots\ldots\ldots\ldots\ldots \quad (21)$$

where $K = \frac{eB_0\lambda_u}{2\pi mC}$ is a dimensionless parameter called the deflection parameter. So Eqs. 18 and 19 becomes:

$$x'(s) = \frac{K}{\beta\gamma} cos(k_u s)$$

$$x(s) = \frac{K}{\beta\gamma k_u} sin(k_u s) \quad \ldots\ldots\ldots\ldots\ldots\ldots \quad (22)$$

For relativistic electrons, ($\beta = 1$), then we get:

$$x'(s) = \frac{K}{\gamma} cos(k_u s)$$

$$x(s) = \frac{K}{\gamma k_u} sin(k_u s)$$

The above equations represent the trajectory of the electron motion through undulator, the maximum value of the trajectory angle as:

$$x'_{max} = \theta = \frac{K}{\gamma}$$

It leads to a difference between wigglers and undulators as follows:

$$\begin{cases} k \leq 1\theta \leq \frac{1}{\gamma} (undulator) \\ k > 1\theta > \frac{1}{\gamma} (wiggler) \end{cases}$$

Now, we need to find the relative transverse velocity in the direction of x:

$$\beta_x = \frac{dx/dt}{c} = \frac{K}{\gamma} cos(k_u s) \quad \ldots\ldots\ldots\ldots\ldots\ldots \quad (23)$$

The change in relative transverse velocity causes a change in a relative longitudinal velocity β_s while the relative velocity β_z is zero,

So, the total relative velocity β is:

$$\beta^2 = \beta_x^2 + \beta_s^2 \quad \ldots\ldots\ldots\ldots\ldots\ldots \quad (24)$$

Plugging Eq. 23 into Eq. 24, we get:

$$\beta^2 = \frac{K^2}{\gamma^2} cos^2(k_u s) + \beta_s^2 \quad \ldots\ldots\ldots\ldots\ldots\ldots \quad (25)$$

It leads to,

$$\beta_s^2 = \beta^2 - \frac{K^2}{\gamma^2} cos^2(k_u s) \quad \ldots\ldots\ldots\ldots\ldots\ldots \quad (26)$$

To find β_s we use the identity: $2cos^2 A = 1 + cos(2A)$

$$\beta_{s=}^2 \beta_-^2 \frac{K^2}{\gamma^2}\left[\frac{1}{2} + \frac{1}{2} cos(2k_u s)\right] \quad \ldots\ldots\ldots\ldots\ldots\ldots \quad (27)$$

It finally leads to:

$$\beta_s = \beta\left(1 - \frac{K^2}{4\beta^2\gamma^2}\right)$$

$$\beta_s \cong 1 - \frac{1}{2\gamma^2}\left(1 + \frac{k^2}{2}\right) \quad \ldots\ldots\ldots\ldots\ldots\ldots \quad (28)$$

2.3.2 Resonance Wavelength of undulator radiation

Figure A.13 (see appendix A) shows the interference process of the electron beam from point A to point B and the radiation is observed at an angle θ with respect to the path of the electron.

The distance traveled by the wave is c τ with c is speed of light and τ is the periodic time. The distance while travelled by the electron during the same time is λ_u cos(θ). So, the difference in the two distances is

$$d = c\,\tau - \lambda_u \cos(\theta) \quad \ldots\ldots\ldots\ldots\ldots\ldots \quad (29)$$

substituting for the periodic time $\tau = \frac{\lambda u}{\beta_s c}$ and the distance over n period $d = n\lambda_n$ into Eq.29, we obtain:

$$n\lambda_n = \frac{\lambda_u}{\beta_s} - \lambda_u cos\theta \quad \ldots\ldots\ldots\ldots\ldots\ldots \quad (30)$$

$$n\lambda_n = \lambda_u\left[\frac{1}{\beta_s} - cos\theta\right] \quad \ldots\ldots\ldots\ldots\ldots\ldots \quad (31)$$

By using this identity: $1 - cos\theta = 2sin^2(\theta\ /\ 2)$, in Eq. 31, we get,

$$n\lambda_n = \lambda u\left[\frac{1}{\beta_s} - 1 - 2sin^2(\theta/2)\right] \quad \ldots\ldots\ldots\ldots\ldots\ldots \quad (32)$$

Now, inserting $sin\theta \cong \theta$ due to the very small emission angle:

$$n\lambda_n = \lambda u\left[\frac{1}{\beta_s} - 1 - \frac{2\theta^2}{4}\right] \quad \ldots\ldots\ldots\ldots\ldots\ldots \quad (33)$$

Substituting for β_s from eq'n 28 in eq'n 33:

$$n\lambda_n = \lambda u\left[\frac{1}{1-\frac{1}{2\gamma^2}\left(1+\frac{k^2}{2}\right)} - 1 - \frac{\theta^2}{2}\right] \quad \ldots\ldots\ldots\ldots\ldots\ldots \quad (34)$$

Putting $x = \frac{1}{2\gamma^2}\left(1 + \frac{K^2}{2}\right)$, Eq. 34 becomes

$$n\lambda_n = \lambda u\left[\frac{1}{1-x} - 1 - \frac{\theta^2}{2}\right]$$

$$n\lambda_n = \lambda u\left[(1-x)^{-1} - 1 - \frac{\theta^2}{2}\right] \quad \ldots\ldots\ldots\ldots\ldots\ldots \quad (35)$$

Using $(1-x)^{-1} \cong 1 + x$, we simplify as

$$n\lambda_n = \lambda u\left[1 + x - 1 - \frac{\theta^2}{2}\right]$$

$$n\lambda_n = \lambda u\left[x - \frac{\theta^2}{2}\right] \quad \ldots\ldots\ldots\ldots\ldots\ldots \quad (36)$$

In Substituting the value of x, we obtain

$$n\lambda_n = \lambda u\left[\frac{1}{2\gamma^2}\left(1 + \frac{k^2}{2}\right) - \frac{\theta^2}{2}\right]$$

Multiplying $\frac{\theta^2}{2}$ by $\frac{\gamma^2}{\gamma^2}$, the resonant wavelength becomes

$$\lambda_n = \frac{\lambda_u}{2n\gamma^2}\left[1 + \frac{K^2}{2} + \theta^2\gamma^2\right] \ldots\ldots\ldots\ldots\ldots\ldots \quad (37)$$

This equation calculates the wavelength of radiation emitted by the undulator for the nth harmonics. The radiation spectrum is composed of a series of harmonics, each emitted at

a particular wavelength λ_n. Odd harmonics are due to on-axis emission and are high intensity, while even harmonics (off-axis emission) are less intense.

Odd harmonics arise when the radiation from oscillating electrons interferes in a manner that reinforces only the odd multiples of the fundamental frequency, (such as the 1st, 3rd, and 5th harmonics). This occurs due to the special symmetry in the electron's motion and its emission of radiation. This symmetry has a significant effect on on-axis emission, where radiation is emitted along the direction of the electron's movement. In this case, the interference pattern of the radiation waves naturally favors the odd harmonics, as they constructively interfere along the axis, while even harmonics are suppressed or canceled out.

In contrast, for off-axis emission, the situation changes. At finite observation angles, the symmetry responsible for canceling the even harmonics is broken. Consequently, both odd and even harmonics can appear in the radiation spectrum, although the odd harmonics generally remain stronger.

Chapter Three

Radiation from Insertion Devices

When the electron beam passes through the undulator, it follows a sinusoidal trajectory and emits electromagnetic radiation called synchrotron radiation. This chapter discuss the main parameters of synchrotron radiation and gives a detailed theoretical background of each parameter.

3.1 Photon Beam Brightness

The brightness indicates the photon flux (number of photons per second) per unit electron source size and angular divergence. The brightness is giving by is:

$$Brightness = \frac{F}{4\pi^2 \Sigma_x \Sigma_{x'} \Sigma_z \Sigma_{z'}} \quad \text{..... (38a)}$$

Where F is the photon flux and $4\pi^2 \Sigma_x \Sigma_{x'} \Sigma_z \Sigma_{z'}$ stands for the phase space volume occupied by the photon beam.

Hence, the Σ_x , Σ_z and $\Sigma_{x'}$, $\Sigma_{z'}$ can be calculated by a combination of the size of the electron beam and the size of the photon beam respectively that emitted by single electron as shown below:

$$\Sigma_{x,z} = \sqrt{\sigma_{x,z}^2 + \sigma_{x,z(p)}^2}$$

$$\Sigma_{x',z'} = \sqrt{\sigma_{x',z'}^2 + \sigma_{x',z'(p)}^2} \quad \text{..... (38b)}$$

3.2 Electron Beam Size and Emittance

The photon beam size of the emitted radiation can approximate to follow a Gaussian distribution, the horizontal and vertical directions and its angular divergence in each direction. The horizontal beam size σ_x and the divergence $\sigma_{x'}$ are:

$$\sigma_x = \sqrt{\varepsilon_x \beta_x + (\eta_x \cdot \sigma_e)^2} \quad \text{..... (39a)}$$

$$\sigma_{x'} = \sqrt{\frac{\varepsilon_x}{\beta_x} + (\eta_{x'} \cdot \sigma_e)^2} \quad \text{..... (39b)}$$

where β is the betatron amplitude function.

However, the vertical beam size σ_z and its divergence $\sigma_{z'}$ are:

$$\sigma_z = \sqrt{\varepsilon_z \beta_z} \quad \ldots\ldots\ldots\ldots\ldots\ldots \quad (40a)$$

$$\sigma_{z'} = \sqrt{\frac{\varepsilon_z}{\beta_z}} \quad \ldots\ldots\ldots\ldots\ldots\ldots \quad (40b)$$

where ε is the emittance and β is the betatron amplitude function.

On the other hand, the size of the electron beam times the angular distribution of the radiation which is called the angular divergence.

$$\epsilon_x = \sigma_x \cdot \sigma_{x'} \quad \ldots\ldots\ldots\ldots\ldots\ldots \quad (41)$$

3.3 Betatron Oscillation and Energy Spread

As a result of energy loss due to photon emission, the electron will follow a new orbit. Therefore, to bring back the electron to its reference trajectory, the quadrupole magnets are installed in the storage ring to focus in the horizontal and vertical planes by applying a recoil force on the electron to oscillate around the synchronous orbit and this oscillation is called betatron oscillations.

To well describe the horizontal and vertical oscillations we define a betatron amplitude functions β_x and β_z. Thus, the horizontal $x(s)$ and vertical $Z(s)$ amplitudes:

$$x(s) = \sqrt{a\beta_x(s)}cos(\psi_x(s) + \phi_x)$$

$$Z(s) = \sqrt{b\beta_z(s)}cos(\psi_z(s) + \phi_z) \quad \ldots\ldots\ldots\ldots\ldots\ldots \quad (42)$$

where $a\ and\ b$ are the horizontal and vertical initial amplitudes,

ϕ_x and ϕ_z: are constants and defined by the initial conditions.

$\psi_x(s)$ and $\psi_z(s)$: are the horizontal and vertical phase advance of betatron oscillations respectively.

The deviation of electrons from the energy of the synchronous particle is a result of the

energy oscillations around the synchronous orbit as shown in figure A.14 (see appendix A). Therefore, we have a difference in energy ΔE from the nominal energy E and the electron which has a positive difference follows a long-closed orbit and gain less energy from RF Cavity. On the other hand, the electron which has a negative difference follows a short orbit and gains higher energy from RF Cavity as represented by that:

$$\frac{\Delta l}{l} = \alpha \frac{\Delta E}{E} \quad \ldots\ldots\ldots\ldots\ldots\ldots \quad (43)$$

where α is a constant called the momentum compaction factor, l is the path length that the synchronous particle is travelled at nominal energy and Δl is the difference in the path length of synchronous orbit due to energy difference from the nominal energy.

Thus, this leads to present trajectory difference Δx(s) with relative to the original trajectory of the synchronous particle x(s) as given by:

$$\Delta x(s) = \eta_{\mathrm{x}}(s) \frac{\Delta E}{E} \quad \ldots\ldots\ldots\ldots\ldots\ldots \quad (44)$$

where, $\eta_{\mathrm{x}}(s)$ is the dispersion function.

Furthermore, assuming that the energy of the electron in the bunch follows a Gaussian distribution, as shown in figure A.15 (see appendix A), and the standard deviation σ_E and nominal energy E, the energy spread is given by:

$$\sigma_e = \frac{\sigma_E}{E} \quad \ldots\ldots\ldots\ldots\ldots\ldots \quad (45)$$

Chapter Four

Photon flux and brightness of synchrotron radiation emitted by the undulator U20

The figure of merit of synchrotron radiation is the photon beam brightness. Different scientific applications require high brightness radiation. For example, in protein crystallography, high brightness is needed to resolve the different diffraction orders [32]. In spectroscopy experiments, sub-μm spatial resolution is needed which requires small source size and angular divergence [33]. To obtain high brightness we need high flux and small source size and divergence (beam emittance). Therefore, we study synchrotron radiation emitted by undulators for different beam emittances. Reducing the emittance is the way to increase the brightness. We also study the effect of energy spread.

In this chapter, the photon flux emitted by the U20 undulator is calculated as a function of photon energy for harmonics (from n=1 to n=11) for the ideal conditions (zero emittance and zero energy spread), in addition to some values of emittance and energy spread, and the effect of emittance and energy spread on the photon flux. This is important for the photon beam brightness, calculated by the photon flux with the effects of the beam emittance.

4.1 SRW software

The Synchrotron Radiation Workshop (SRW) [34] is a software tool used in this chapter to calculate the photon beam flux and brightness of synchrotron radiation. SRW is used to calculate the spectrum of insertion devices radiation depending on the main parameters of the insertion itself: magnetic field, period and taking into account the main parameters of the electron beam: the beam emittance, the energy spread. It considers also the physical aperture through which the radiation is collected.

4.2 The undulator U20

The U20 undulator has already been installed in other synchrotrons and has proven important spectral performance. This thesis considers the U20 proposed in SOLEIL [35], shown in figure A.16 (see appendix A), to examine the photon beam flux and brightness for the current and the potential future lower emittance and energy spread for SESAME.

The U20 is composed of 98 periods each of 20 mm period length. It uses hybrid permanent magnet technology. which is composed of permanent magnets with alternative polarities with poles made of conducting material inserted between the magnets. The poles concentrate the magnetic flux and thus enhance the magnitude of the magnetic field. The hybrid permanent magnets provide higher magnetic field for the small gap (5.5 mm) and higher magnetic remanence and higher peak field. Table 2 shows the main parameters of period, length, gap and technology for the undulator U20.

Table 2

The main parameters of undulator U20

Parameter	Value
Period λ_u [mm]	20
Length L[m]	1.96
Gap g[mm]	5.5-30
Technology	Permanent magnet

Note: [36].

Table 3 shows the main parameters of SESAME storage ring as communicated to us by SESAME to carry out this work.

Table 3

The main parameters for SESAME

Parameter	Value
Energy	2.5 GeV
Current	400 mA
Vertical magnetic field B_z	0.95 T
Circumference	133.2 m
Number of buckets	222
Horizontal emittance	26nm. rad
Coupling coefficient	~ 0.4%
Energy spread	0.1703%
β_x	13.59 m
β_z	1.65 m
$\alpha_{(x,z)}$	0
η_x	0.533 m
$\eta_{x'}$	0
η_z	0
$\eta_{z'}$	0

Note: [7].

4.3 Photon flux for zero emittance and zero energy spread

Figure 1 shows the flux emitted by the undulator U20 as a function of photon energy. The spectrum is composed of a series of harmonics, each harmonic results from a given resonance frequency, the first (fundamental) harmonic is the result of the fundamental resonance frequency and so on. The ideal conditions of zero emittance and zero energy spread result in the presence of only odd harmonics, while the even harmonics are suppressed. As the harmonic number increases, the intensity decreases. H1 is obviously more intense than H11 because slow oscillations produce lower order harmonics, whereas rapid oscillations, which are harder to maintain, produce higher order harmonics.

In the case of zero emittance and zero energy spread, the electron beam is perfectly collimated, with no spread in transverse position or angle, which results in an emission pattern that contains odd harmonics. Additionally, with zero energy spread, all electrons in the beam have the same energy, leading to a consistent on-axis emission. According to the undulator resonance condition (eq. 37), the emitted radiation is concentrated at discrete wavelengths λ_n that is inversely proportional to the harmonic number n. On axis emission ($\theta = 0$) generates radiation at the odd harmonics (1st, 3rd, 5th, etc.), while even harmonics are suppressed due to the planar undulator symmetry.

Figure 1

Photon flux as a function of energy of synchrotron radiation emitted by the undulator U20 for zero emittance and energy spread

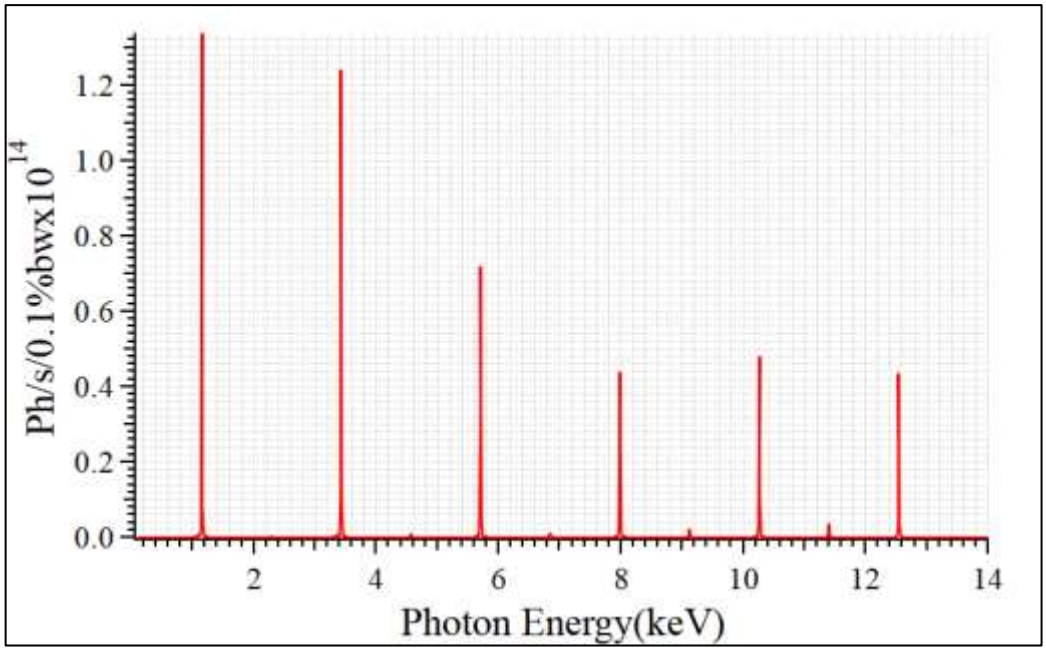

Referring to equation (37) the resonance wavelength for the fundamental harmonic n=1 of the U20 undulator is calculated as $\lambda_1 = 1.14nm$, where the Lorentz factor $\gamma = 4892$ for SESAME, and the deflection parameter $K = 1.86$. This corresponds to a resonance photon energy of E_1= 1.089keV. This theoretical value is in very good agreement with the position of the first harmonic peak shown in Figure 1, confirming the validity of the obtained results.

4.4 Effect of the emittance on the photon flux emitted by the U20 undulator

Figure 2 shows the flux emitted by the undulator U20 as a function of photon energy collected through an aperture of 0.1 mm x 0.1 mm located 10 meters away from the source calculated for beam energy of 2.5 GeV, beam current of 400 mA and energy spread of 0.1703×10^{-2} for different horizontal emittances. The graph includes a zoom-in view on the harmonics H1, H2, H10, and H11. The X-axis shows the photon energy (in KeV) with photon energies ranging from (0.1 KeV to 14 KeV). The Y-axis displays the flux in photons/s. Figure 2 shows that in realistic conditions (non-zero emittance and non-zero energy spread), finite beam emittance and energy spread generate even harmonics, broaden and reduce the peak intensity of all harmonics.

In this study, the focus will be on the H1, H2, H10, and H11 harmonics because we need to study the excerpt: the lower order harmonics of odd (H1) and even (H2). We also need to examine the higher order harmonics (H10 and H11). Users are interested in the odd harmonics, and the fundamental usually contains more flux. On the other hand, other applications need higher energy, for this reason, we go to a higher order harmonic.

Figure 2

Photon flux as a function of emitted energy from the U20 undulator, for various values of horizontal emittance with 0.1703% energy spread

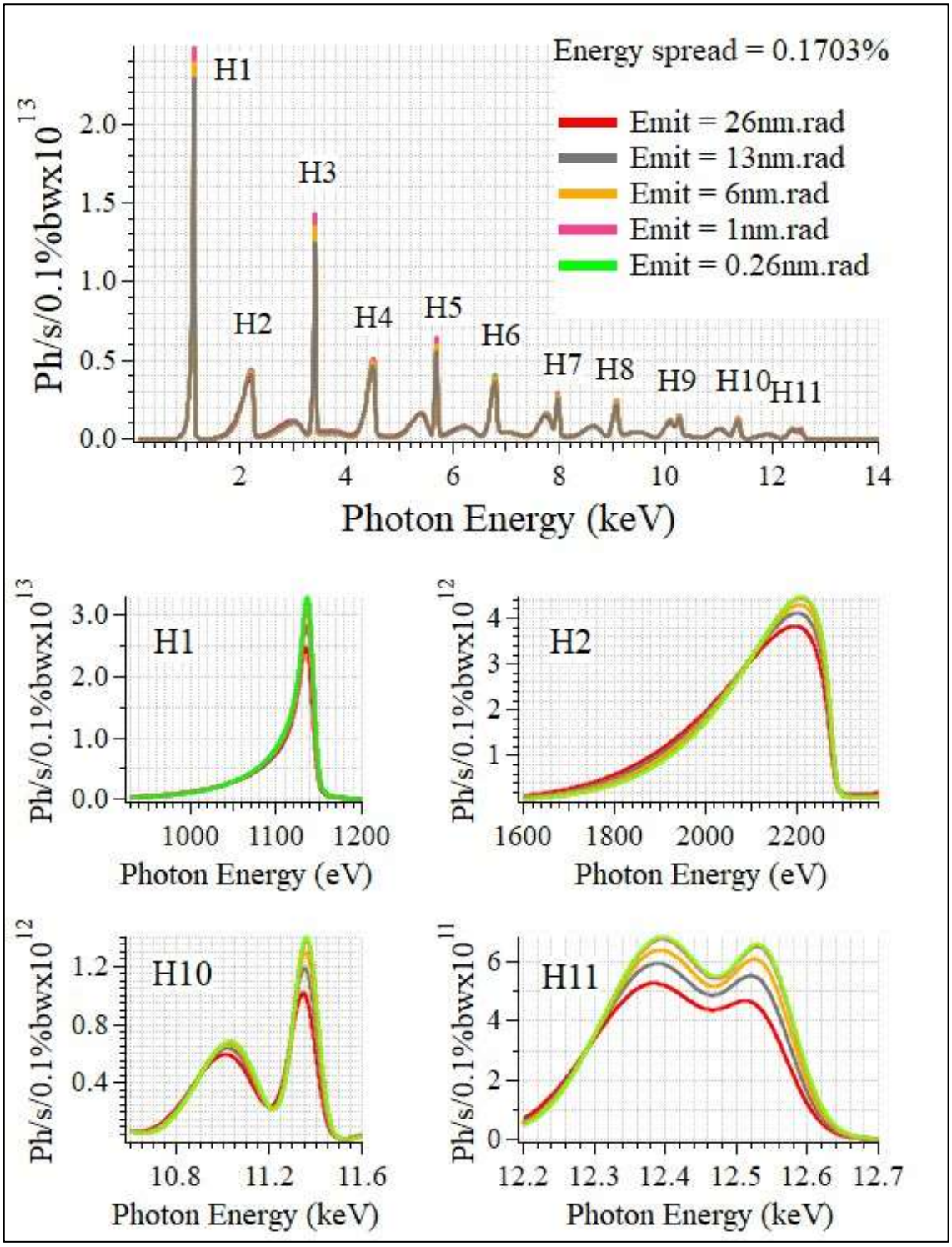

With non-zero emittance, the electron beam has a finite angular spread due to partially constructive interference from electrons at different angles, leading to a decrease in flux. As a consequence, the harmonic peaks become broader and less sharp compared to the case with zero emittance. The overall photon flux collected through the fixed aperture decreases because part of the radiation falls outside the angular acceptance. By decreasing the emittance, the radiation becomes more collimated, and the harmonic peaks appear narrower and more intense, which results in an increase in the collected flux.

The influence of emittance is stronger at higher order harmonics. Introducing the definition of relative flux gain G= $\frac{\Delta f}{f} \times 100\%$, where Δf is the change in the flux of a given harmonic by decreasing the horizontal emittance from 26 nm.rad to 0.26 nm.rad, it is found that the intensity of the first harmonic increases by 33% by reducing the horizontal emittance from 26 nm.rad to 0.26 nm.rad and the intensity of eleventh harmonic increases by 29%. Table 4 shows the flux gain calculation for different harmonics. The flux of higher-order harmonics drops rapidly with emittance.

Table 4

Flux gain of the U20 undulator spectrum as the emittance decreases

Harmonic	flux gain
Fundamental (n=1)	33%
n=2	16%
n=10	40%
n=11	29%

Odd harmonics are less sensitive to emittance reduction compared to even harmonics which are suppressed on-axis because of destructive interference. Therefore, in the U20 undulator spectrum with decreasing emittance, odd harmonics remain intense, while the intensity of even harmonics decreases more sharply.

Diffraction limited is the lowest possible emittance for the harmonic and is defined by $\frac{\lambda_n}{4\pi}$ [37]. The overall emission behavior is either emittance dominated or diffraction limited.

If the emittance of the electron beam is less than or equal to the diffraction limited value, then the U20 undulator operates in the diffraction-limited mode, where the radiation is

totally in constructive interference. In this case, the spectrum shows only one sharp peak. Conversely, if the beam emittance is much greater than the diffraction limit, then the U20 undulator operates in the emittance dominated mode, with only partial constructive interference due to differences in the angular phase of the electrons. This case may appear as a double peak structure, particularly for higher harmonics such as H10 and H11. Table (5) shows the comparison between the diffraction limited emittance and the beam emittance (26 nm.rad) for the selected harmonics (H1, H2, H10, and H11).

Table 5

Comparison between the diffraction limit and the beam emittance (26nm.rad) for the U20 undulator

Harmonic (n)	λ_n (nm)	Diffraction limit (nm)
1	1.14	0.09
2	0.57	0.045
10	0.114	0.009
11	0.1	0.008

From the table, it is clear that for all harmonics the U20 operates in the emittance dominated mode because the beam emittance (26nm.rad) is much higher than the diffraction limited emittance (column 3 in table 5). In this system, the radiation emitted from different electrons is not perfectly in phase, because each electron follows a slightly different trajectory and radiates under a different angle. As a result, the on-axis constructive interference becomes weaker.

For the fundamental harmonic (H1), this loss of coherence causes the on-axis radiation to become broader but still appear as a single peak, because the radiation cone is sufficiently wide to include the small angular deviations introduced by the beam emittance.

For even harmonics (H2), the planar undulator symmetry cancels the on-axis radiation completely, and therefore no central peak is observed. However, for the higher harmonics (H10 and H11), the narrower radiation cone, combined with stronger angular phase differences produces two partially separated resonance conditions, leading to the appearance of a double peak structure in the spectral flux distribution.

Figure 2 also shows that decreasing the beam emittance increases the photon flux. Therefore, the U20 undulator goes from operation of the emittance dominated mode to operation of diffraction limited mode due to the value of emittance approaching with the diffraction limited value, and the harmonic peaks become sharper and more intense.

4.5 Effect of the energy spread on the photon flux emitted by the U20 undulator

Figure 3 shows the flux emitted by the undulator U20 as a function of photon energy collected through an aperture of 0.1 mm x 0.1 mm located 10 meters away from the source calculated for beam energy of 2.5 GeV, beam current of 400 mA and horizontal emittance of 26 nm.rad for different energy spreads. The graph also includes a zoomed-in view focusing on the harmonics H1, H2, H10, and H11. The X-axis shows the photon energy (in KeV) with photon energies ranging from (0.1 KeV to 14 KeV). The Y-axis displays the flux in photons/s.

Increasing the energy spread decreases the photon flux of all harmonics and leads to harmonic broadening and the appearance of double peaks at higher order harmonics (H10 and H11).

Figure 3

Photon flux as a function of emitted energy from the U20 undulator, for varying values of energy spread with 26nm.rad emittance

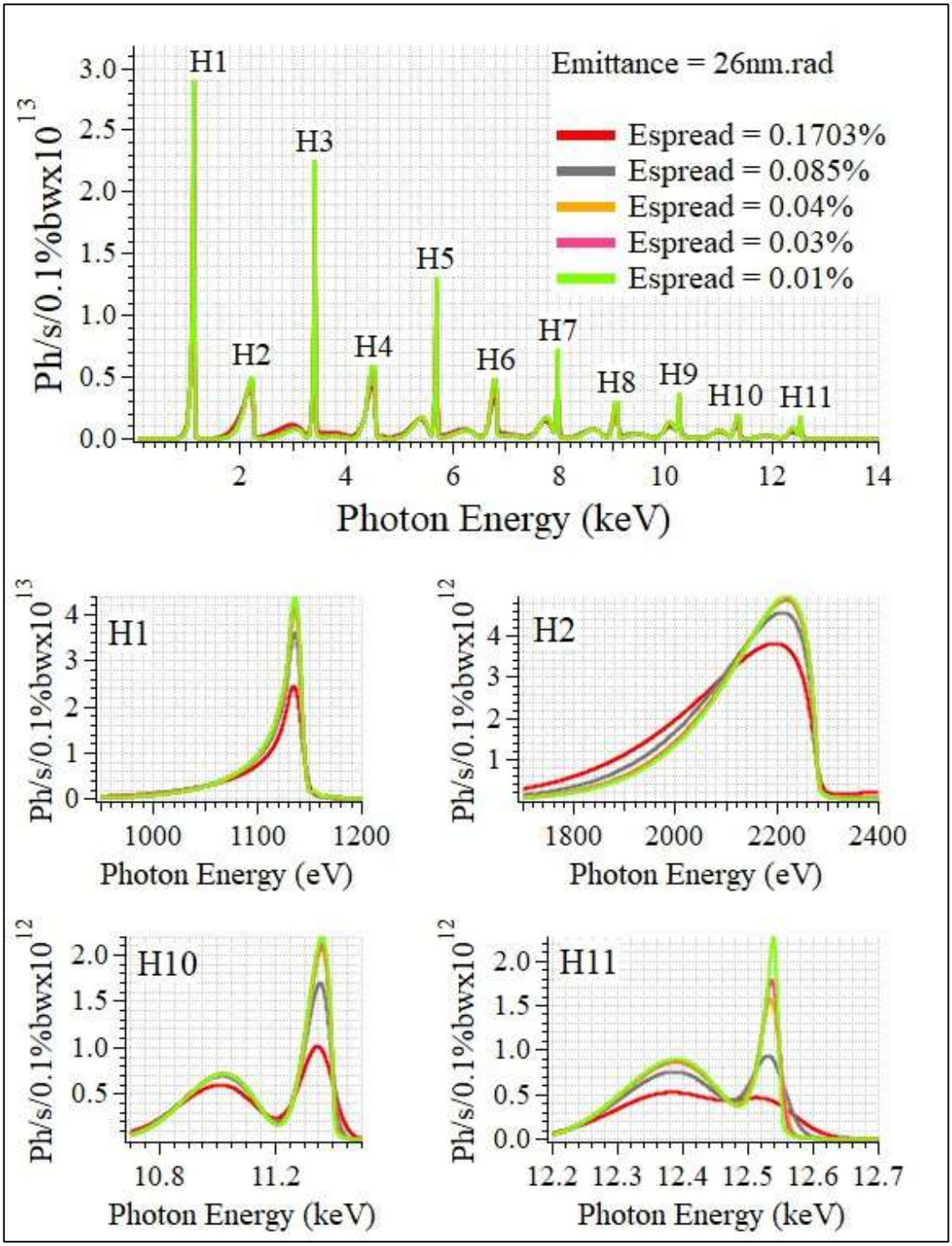

When the electron beam has an energy spread, it means that not all electrons have the same energy and therefore, not the same Lorentz factor (γ). The electrons are distributed around the nominal energy of the beam some slightly above it and some below. As a result, each electron emits radiation at a different wavelength, and the total radiation from the beam is no longer perfectly in phase. This loss of phase coherence weakens the constructive interference that normally forms the on-axis peak, leading to a decrease in flux.

At the same time, the harmonic line becomes wider, which is known as the broadening effect.

For higher harmonics (H10 and H11), a double peak appears instead of a single one. This occurs because the electrons have slightly different energies and therefore radiate at nearby wavelengths. These emissions overlap only partially, resulting in partially constructive interference in the spectrum.

Harmonic broadening can be explained as follows: the harmonic bandwidth Δλ is due to two effects: homogeneous and inhomogeneous broadening. Homogeneous broadening which causes a uniform spread of the energy distribution of each harmonic. It is inversely proportional to the harmonic number n and the number of periods of the undulator N as given by equation (46) [38].

$$\frac{\Delta\lambda}{\lambda} = \frac{1}{n \cdot N} \quad \text{..... (46)}$$

The inhomogeneous broadening also affects the bandwidth of the radiation which occurs when the broadening varies across the electron beam. The inhomogeneous broadening is fixed by the energy spread of the electron beam as shown in equation (47) [39].

$$\frac{\Delta\lambda}{\lambda} = 2\sigma_E \quad \text{..... (47)}$$

The inhomogeneous broadening bandwidth of σ_E = 0.1703% is:

$$\frac{\Delta\lambda}{\lambda} = (2) \cdot (0.001703) = 0.34\%$$

The total broadening is given by:

$$\frac{\Delta\lambda}{\lambda} = \sqrt{\left(\frac{\Delta\lambda}{\lambda}\right)_h^2 + \left(\frac{\Delta\lambda}{\lambda}\right)_{in}^2} \quad \ldots\ldots\ldots (48)$$

In the case of the U20 undulator (N=98 period), the homogeneous, inhomogeneous and total broadening bandwidth of each harmonic under study is calculated and the results are summarized in table 6.

Table 6

The homogeneous broadening for the different harmonics emitted by the U20 undulator

Harmonic (n)	Wavelength (λ)	Homogeneous (%)	Inhomogeneous (%)	Total broadening (%)
n =1	1.14nm	1	0.34	1.076
n =2	0.57nm	0.5	0.34	0.613
n =10	0.114nm	0.1	0.34	0.356
n =11	0.1nm	0.09	0.34	0.353

From the table, it can be concluded that the homogeneous broadening decreases as the harmonic number n increases. On the other hand, the inhomogeneous broadening remains constant for all harmonics since it is independent of n. For the higher harmonics (H10 and H11), it is clear that the inhomogeneous broadening dominates, as its value is very close to the total broadening. At the fundamental harmonic, however, the homogeneous broadening is dominant for the same reason. For n=2, the total broadening value is larger than both the homogeneous and inhomogeneous components, indicating that both terms contribute significantly to the overall line broadening. This confirms that the energy spread sets the lower limit of the spectral bandwidth at high harmonics, as the homogeneous contribution becomes negligible compared to the inhomogeneous term.

4.6 Effect of the emittance on the Brightness emitted by the U20 undulator

Figure 4 shows the brightness emitted by the undulator U20 as a function of photon energy collected through an aperture of 0.1 mm x 0.1 mm located 10 meters away from the source calculated for beam energy of 2.5 GeV, beam current of 400 mA and energy spread of 0.1703×10^{-2} for different horizontal emittances. The X-axis represents the photon energy in keV, while the Y-axis shows the brightness in units of

photons/s/mm²/mr².

Figure 4

Photon beam brightness as a function of photon energy for the U20 undulator, with varying emittance values with 0.1703% energy spread

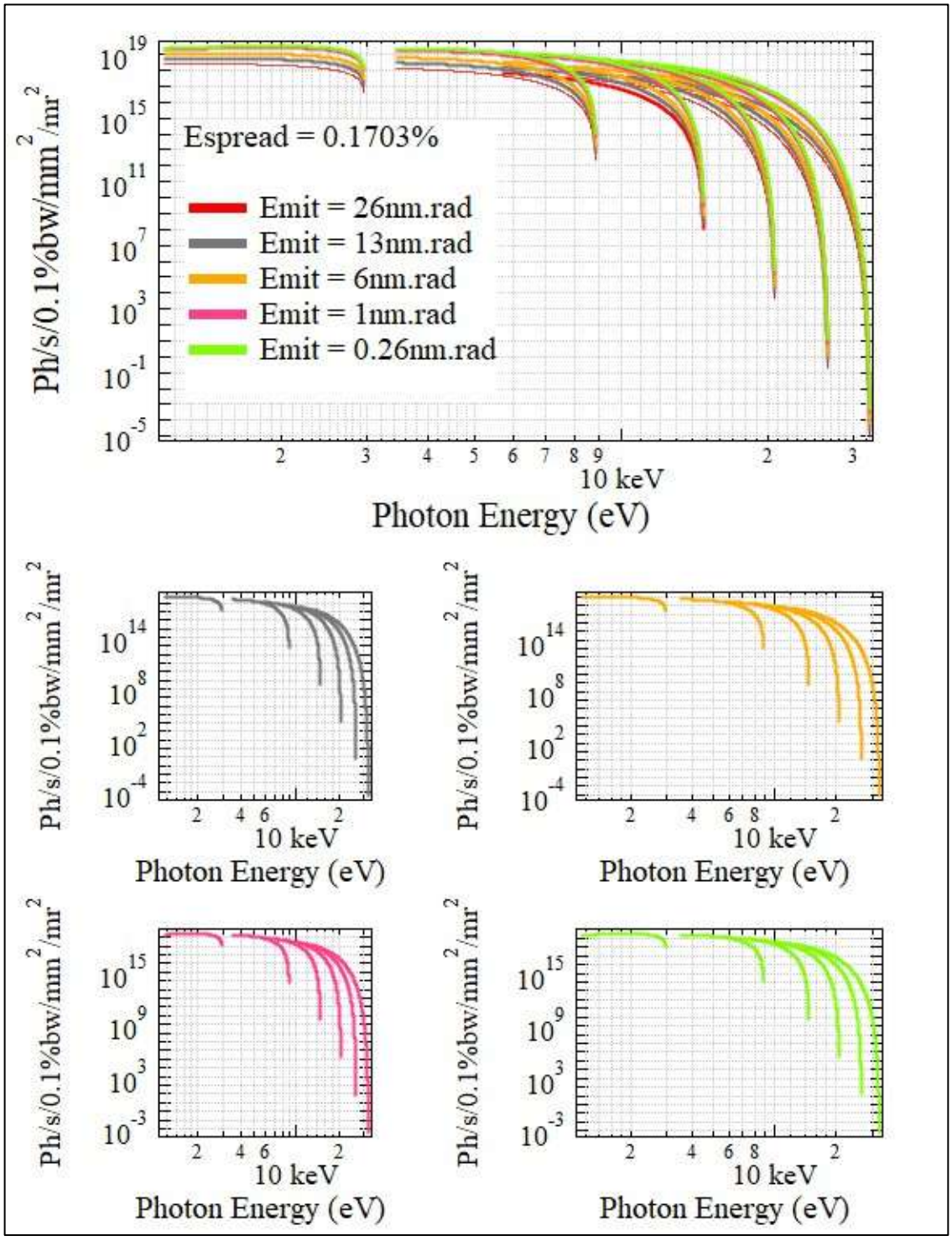

As shown in Figure 4, brightness increases with decreasing emittance. At fundamental

harmonic (H1) of photon energy 1.088 keV, the brightness is at 2.5×10^{18} at emittance 26 nm.rad, while the brightness at emittance 0.26 nm.rad is at 2.15×10^{19}. On the other hand, for the eleventh harmonic (H11) of photon energy 12 keV, the brightness is at 6×10^{15} at emittance 26 nm.rad, while the brightness at 0.26 nm.rad is at 5×10^{17}. This is also explained by the fact that increasing the harmonic number decreases brightness.

Studying the brightness of the U20 undulator is very important because many experiments depend on the brightness of the photon beam. In the U20 undulator, all of the harmonic energies fall within the X-ray region (100 eV-100 keV) in two types of soft and hard, depending on the harmonic number. Soft X-ray of the energy range in X-ray (100 eV-2 keV), important for the experiments that need high brightness at low photon energy as X-ray microscopy. While the hard X-ray range of energy (greater than 5keV) for the experiments that need high brightness at high photon energy as a diffraction experiments [40].

The fundamental harmonic (H1) of energy 1088 eV falls within the range of soft X-rays. The first soft X-ray beamline at SESAME is the Helmholtz SESAME beamline (HESEB), which provides energies up to 1.8 keV for the users [41]. Therefore, the calculated brightness at (H1) falls within the operating range of (HESEB), which makes it suitable for surface-sensitive experiments. On the other hand, the eleventh harmonic (H11) of energy 12 keV falls within the range of hard X-rays. X-ray Absorption Fine Spectroscopy (XAFS) is a beamline at SESAME in the hard X-ray, and it is built on a bending magnet, which provides energies up to 30 keV [42]. However, the U20 undulator proposed in this work provides energy 100 keV with maximum brightness 2.5×10^{18} and maximum flux 2.46×10^{13} at SESAME of emittance 26 nm.rad. Consequently, the energy range of the U20 undulator is not entirely covered by the SESAME beamline, as the SESAME energy range is limited to 30 keV using a bending magnet, which means low flux. In this work, we study even improving more flux and brightness if we decrease the emittance in high energy range.

This study is important for the experiments because it indicates which harmonics can be used and which remain outside the range. Therefore, the brightness analysis not only characterizes the undulator's performance but also determines the scientific importance of each harmonic for real beamline applications.

4.7 Conclusion

This study examined the photon flux and brightness of synchrotron radiation emitted by the U20 undulator under the influence of the beam emittance and energy spread. Brightness is the most important parameter to characterize synchrotron radiation. The results were taken from the synchrotron radiation workshop (SRW) software, depending on the main parameter of the U20 undulator.

Firstly, it begins with the calculations of the photon flux under ideal conditions of zero emittance and zero energy spread, and it was found that the spectrum is composed of a series of harmonics at different resonance frequencies, with only odd harmonics appearing due to the on-axis emission, while the even harmonics are suppressed due to the planar undulator symmetry. It was also found that the relationship between the intensity and the harmonic number is inversely proportional.

Secondly, the effect of the emittance on the photon flux was studied in realistic conditions of non-zero emittance and non-zero energy spread, where the even harmonics appear, and the effect of the emittance is shown by broadened harmonics and a reduction of the peak intensity of harmonics. The focus was on H1, H2, H10, and H11 harmonics. An increase in the beam emittance leads to a decrease in flux due to the angular spread of the electron beam. At high-order harmonics (H10 and H11), the double peak appears due to a decrease in the emission angle of the photon beam, each electron in the beam deviates at a different angle, and it has a different resonance frequency.

Third, the effect of the energy spread on the photon flux, the increase in the energy spread leads to a decrease in the photon flux of all harmonics. Therefore, it will broaden harmonics, and a double peak may appear, especially for higher-order harmonics. The presence of energy spread in the electron beam causes each electron to have a different value of energy, leading to the electrons being distributed around the nominal energy. Consequently, the photon flux decreases, and a double peak appears in high-order harmonics.

Finally, the effect of the emittance on the brightness emitted by the U20 undulator is linked to the photon flux and the beam emittance (source size and divergence). As the flux increases, the brightness increases. On the other hand, brightness decreases with an

increase in the beam emittance, and a reduction in the brightness appears larger at high-order harmonics with high photon energy.

Many different applications need a high brightness, as in protein crystallography and spectroscopy, and other experiments. This occurs by decreasing the emittance, and therefore increasing in flux. As a result, the world goes towards decreasing emittance, and this is very important for synchrotrons for many future applications.

Chapter Five

Design and study of the S-Bend dipole magnets of PERLE accelerator

5.1 Powerful Energy Recovery LINAC for Experiments (PERLE)

PERLE is an Energy Recovery LINAC (ERL) accelerator [43] in Orsay in France with three acceleration and three deceleration turns with maximum beam energy of 500 MeV for the second phase and 250 MeV for the first phase and 20 mA average current. Figure A.17 (see appendix A) shows a top view of the PERLE accelerator which has racetrack dimensions 29 m× 5.5 m× 0.9 m and 45 cm vertical space. It consists of LINAC of two cryomodules with Four 5-cell cavities, six arcs that contain dipoles and quadrupoles, and a spreader/combiner to connect LINAC with arcs sections.

Table 7 shows the basic parameters of PERLE.

Table 7

Main parameters of the PERLE accelerator (500 MeV version)

Parameter	Value
Injection energy (MeV)	7
Max. beam energy (MeV)	500
Average beam current (mA)	20
Bunch charge (pC)	500
Bunch length (mm)	3
Bunch spacing (ns)	25
Normalized emittance (mm. mrad)	6
RF frequency (MHz)	801.58

Figure A.17 (see appendix A) shows the acceleration and deceleration turns of PERLE. A 7 MeV electron beam is injected into the cryomodules that contain the RF- cavities to be accelerated up to 171 MeV for turn 1, 336 MeV for turn 2, and 500 MeV for turn 3.

The beam is then decelerated over 3 turns. A half RF wavelength is added to arc 6 give the beam 180˚phase shift with respect to the RF field after reaching the maximum energy. The electrons are decelerated with a gradient of 82 MV to be dumped at 7 MeV.

5.2 Magnetic system of PERLE

PERLE adopts electromagnetic technology for magnets. A magnet system is an essential part of the PERLE components, which is also important in this research. Usually, in accelerators, a multipole order is used, such as dipoles, quadrupoles, sixtuples, and other components. Still, in this case, PERLE will take the linear elements, dipoles to bend the electron beam, and quadrupoles to focus the electron beam in one plane.

Referring to Figure A.17 (see appendix A), the magnets exist in two parts: spreader/ combiner and arcs. Figure A.18 (see appendix A) shows the magnets of the spreader / combiner and arcs sections.

Figure A.19 (see appendix A) shows the trajectory of the S- bend magnet in the spreader/ combiner section.

Basically, there are 2 families of the S-Bend. S-Bend with a length of 33 cm in arcs (1,2,3) and S-Bend with a length of 66 cm in arcs (4,5,6) as shown in Figure A.20 (see appendix A). This work will consider the design of an S-Bend with a length of 33 cm located in arcs (1,2,3) with maximum magnetic field B = 1.342 T.

Table 8 shows the main characteristics of the S- bend magnets in the spreaders as shown in Figure A.19 and in the arcs as shown in Figure A.20.

Table 8

The main characteristics of the S Bend dipoles in the spreaders and the arcs as defined by the beam dynamics study for 500 MeV

	Location	Name	No.	E [MeV]	L [cm]	B [T]	α [°]	α [rad]
ARCs	Arc1	bAA1	6	89	33	0.472	30	0.524
	Arc2	bAA2	6	171		0.907		
	Arc3	bAA3	6	254		1.342		
	Arc4	bAA4	6	336	66	0.888	30	0.524
	Arc5	bAA5	6	418		1.106		
	Arc6	bAA6	6	500		1.323		
Spreader & Merger	Spr1, Mrg1	b1S02	2	89	33	-0.472	-30	-0.524
		b1S03	2			0.472	30	0.524
		b1S04	2			-0.472	-30	-0.524
	Spr2, Mrg2	b2S02	2	171	33	-0.907	-30	-0.524
		b2S03	2			0.907	30	0.0524
		b2S04	2			-0.907	-30	-0.0524

When the electron beam enters to the arcs it will be affected with dipole magnets to deviates it from its direction and the quadrupole magnets to focus the beam horizontally and vertically to focus the most of photons about small area, and this is consistent with the previous study about reduction of the beam size and emittance (see eq.39a) to get the required magnetic field. Figure A.21 (see appendix A) shows the electron beam and dispersion function in the arcs section the beam size does not exceed 2 mm at 3σ.

5.3 OPERA Software

Opera Software used in this work to carry out the magnetic design of the S- bend, it is a comprehensive suite for Finite Element Analysis, offering users the capability to conduct simulations of electromagnetic (EM) and electromechanical systems in both 2D and 3D. It is particularly beneficial for designing magnets, electric motors, and similar electrical devices [44].

Within Opera, there are specialized environments for both 2D and 3D pre-processing and post-processing, Its Graphical User Interface (GUI) provides easy access to features that simplify electromagnetics and multi-physics design tasks.

Its precision is particularly crucial for analyzing field homogeneities at the parts-per-million level in particle accelerators. It enables in-depth examination of devices incorporating permanent magnets or superconducting coils.

5.4 Magnet design

5.4.1 Yoke design

Figure A.22 (see appendix A) shows a schematic view of the S-bend dipole, the green part represents the core which is called the yoke and it is made from steel with length 330 mm, width of 373.8 mm, high of 250 mm, and gap 40 mm to maintain the field uniformity, the red part represents the coil of the magnet.

A standard steel 1010 that used in the yoke with B-H curve considered in Figure 5.

Figure 5

B-H curve for the 1010 steel used for the yoke of the S- bend dipole

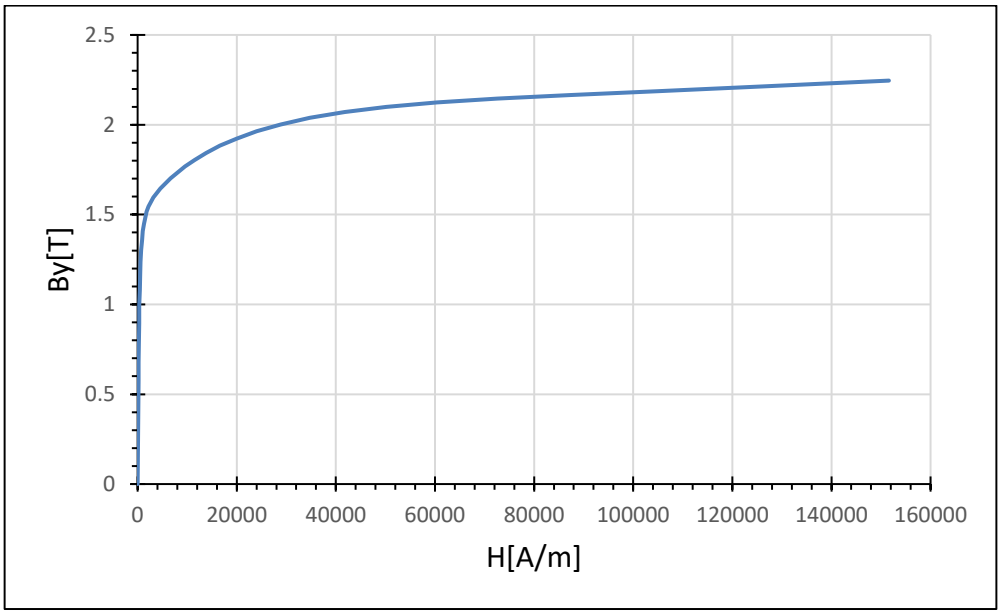

5.4.2 Coil design

Figure 6 shows the coil used in the dipole, a square copper conductor with a 5 mm width, 3 mm inner cavity, and 0.5 mm corner radius, this gives a conductor width of 5.5 mm.

Depending on equation (9), the excitation current of the S- bend magnet is NI = 23000 A.turn with gap h = 40 mm and magnetic field B = 1.342 T. The number of turns for the coil N = 91 arranged in six double pancakes each of 14 turns and one single pancake with 7 turns. Thus, the current through the coil is 252.75 A.

The cross-sectional area of the conductor is $A_{cond.} = (5.5)^2 = 30.25$ mm^2. Therefore, the current density is $J_{coil} = 8.356$ A/mm^2. The current density determines the size of the coil, power consumption, and cooling. To balance between field requirements, technological limits, and operating costs the current density should be optimized in the design process.

Table 9 shows the main parameters of the S- bend dipole magnet depending on these calculations.

Figure 6

The form of the copper conductor used

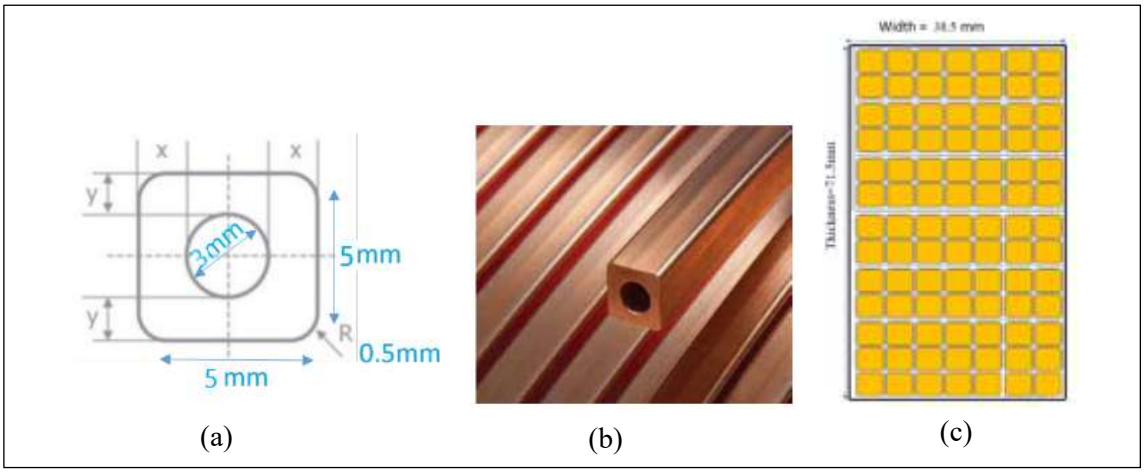

Note: (a) the S- bend dipole, (b) the dimensions of the conductor (c) the cross sectional of the coil.

Table 9

Main parameters for the yoke and coil for S- bend magnet

Parameters	Value
Length of the yoke (mm)	330
High of the yoke (mm)	250
Width of the yoke (mm)	373
gap (mm)	40
Length of dipole (mm)	62.437
Pole width (mm)	80
Magnetic field (T)	1.342
Yoke material	1010 steel
I in the coil (A)	252.75
N (turns)	91
NI (turn. A)	23000
J (A/mm^2)	8.356

The magnetic current value (about 252) A generates non- negligible heating. Therefore, cooling system is needed to prevent magnet heating up.

5.5 magnetic field and dipole analysis

It is crucial to define an adequate boundary around the S-bend dipole magnet where the magnetic field is effectively reduced to zero and to specify which components of the magnetic field are zero at each plane. The S-bend dipole magnet exhibits tangential

magnetic symmetry around the x-y plane, reflecting the uniform curvature and bending of the magnetic field in this plane. Additionally, it shows a varying magnetic field distribution along the z-direction, with symmetry primarily in the z-x plane, where the magnetic field changes due to the bending. The magnetostatic analysis in Opera should account for these symmetries by setting boundary conditions that reflect the decrease of the magnetic field strength away from the central bend region, and ensuring that the field components align with the intended design for steering and beam direction control.

Figure 7 presents the magnetic field distribution in the yoke which is 0.913 T by studying the boundary around the magnet.

Figure 7

Magnetic field distribution in the dipole and the value of the magnetic field at a center of the yoke is 0.913 T

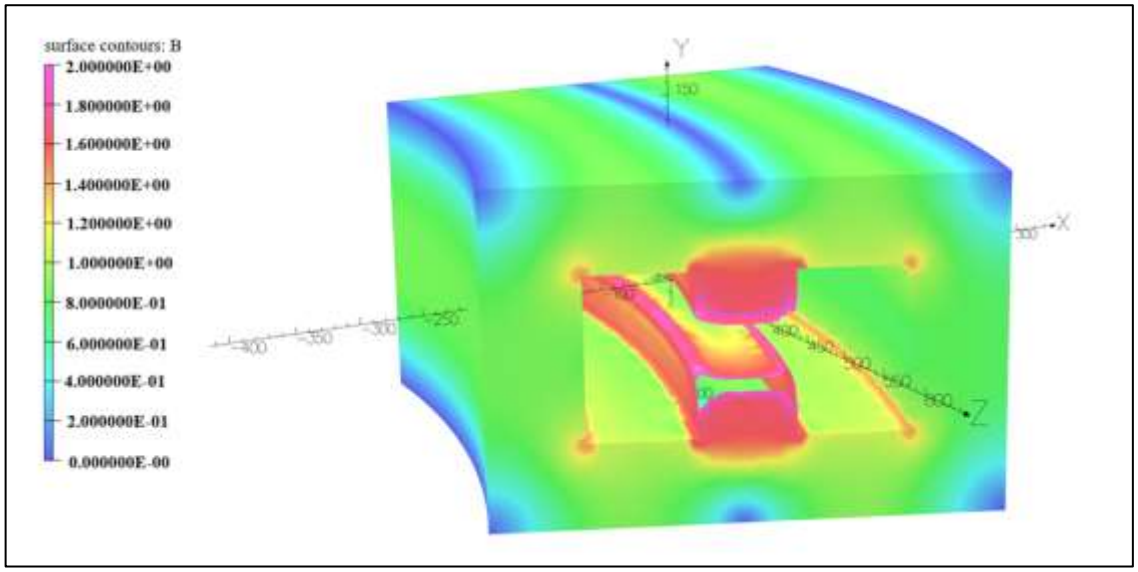

In an S-bend dipole magnet, the magnetic field strength reaches its maximum of 0.94 T (see figure 8) in the center of the curved sections, which is crucial for bending and directing the particle beam. As the arc moves towards the ends of the curved sections and into the straight sections, the field strength gradually decreases, ensuring smooth transitions and precise beam steering.

Figure 9 shows the values of a magnetic field distribution along the longitudinal direction of the beam.

Figure 8

The variation of the magnetic field of the horizontal dimension z and the value of By along the arc passes through the center is -0.94 T

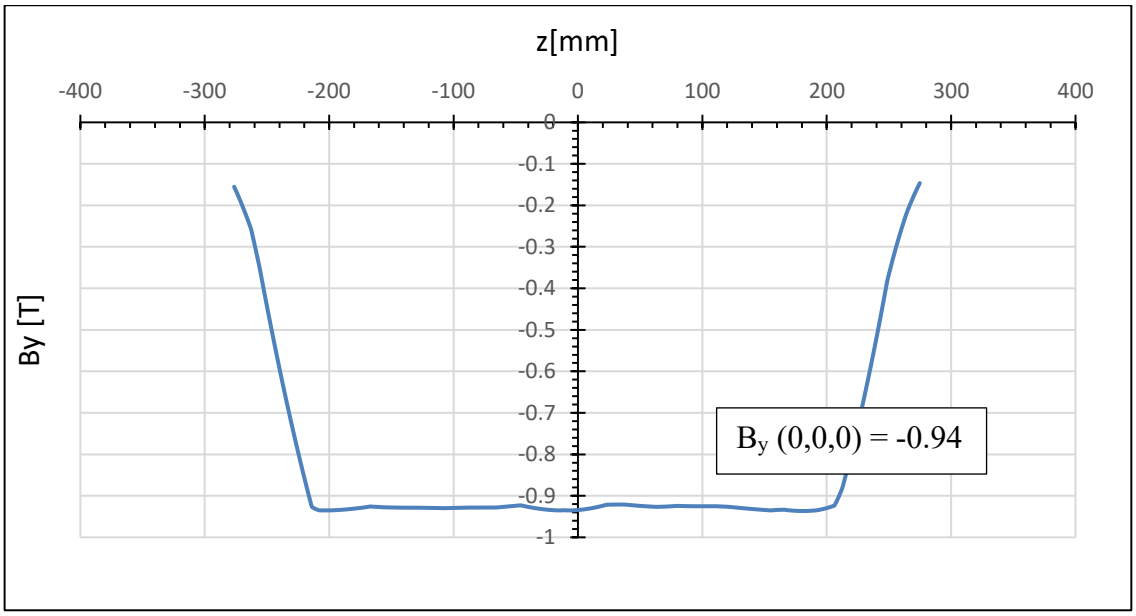

When a straight line is drawn through the center of an S-bend dipole magnet, the magnetic field strength is highest along this line in the central region of the curved sections, reaching up to around 0.94 T (see figure 9). In the straight sections, the field strength decreases, ensuring a smooth transition for the particle beam from the curved to the straight path. This distribution helps in effectively steering and guiding the beam throughout the magnet.

Figure 9 shown the values of a magnetic field distribution along the line due to the center of the dipole.

Figure 9

The variation of the magnetic field with horizontal x direction and the value of By along the line passes through the center is -0.94 T

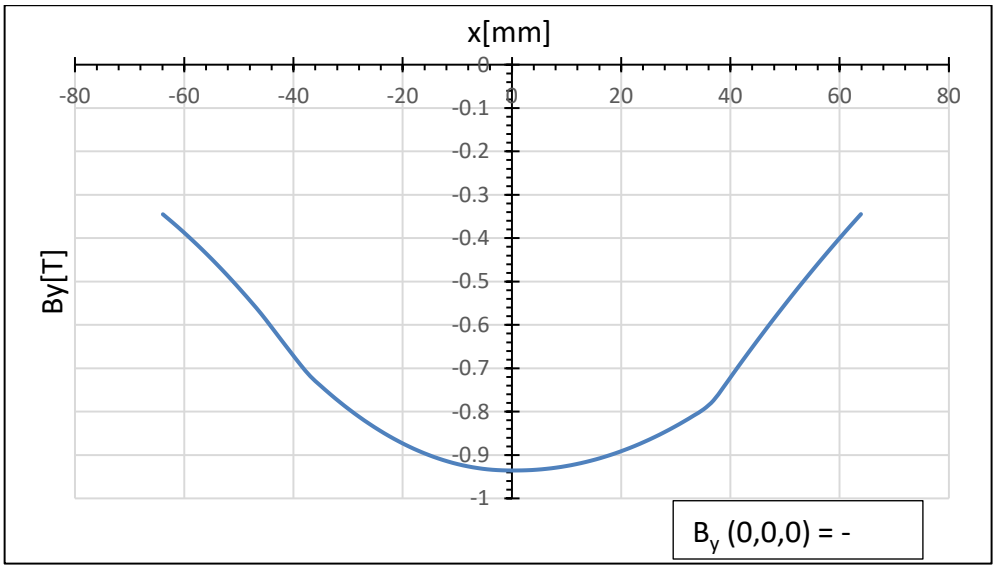

Field homogeneity in the gap along the pole width of an S-bend dipole magnet measures how uniformly the magnetic field is distributed across this space as shown in (figure 10).

Achieving high homogeneity is crucial for consistent beam steering and performance. The design of the poles and careful adjustments ensure that the magnetic field strength and direction are as uniform as possible, leading to precise and reliable operation of the magnet.

Figure 10

Field homogeneity in the gap along the pole width

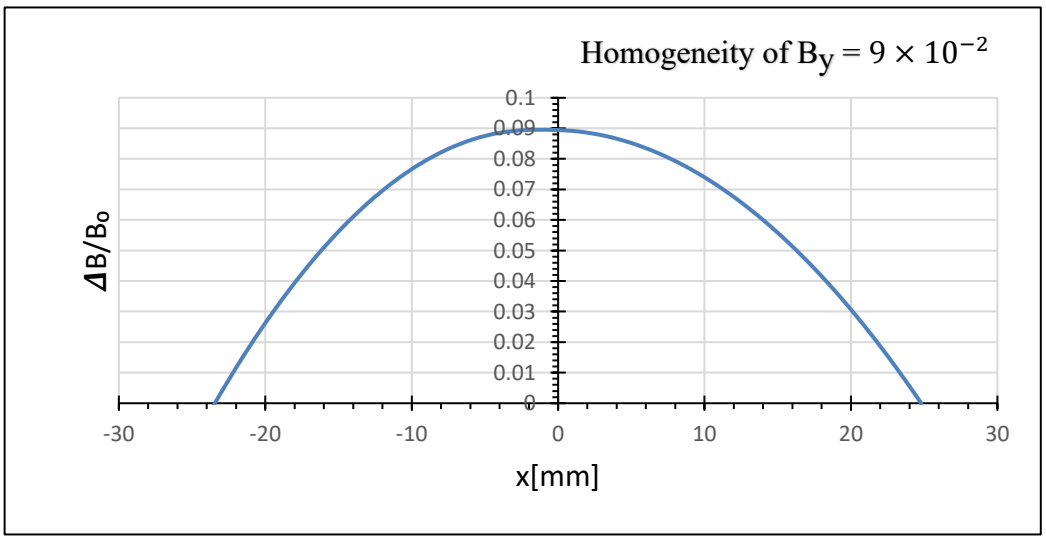

5.6 Cooling system

There are two cooling technologies used in the field of normal-conducting magnets: air cooling and water cooling [45]. Water cooling is considered PERLE due to its superior cooling ability compared to air cooling. The water-cooling system implies considering the accepted values of the current density range between 2 A/mm^2 and 10 A/mm^2 to prevent the increase of temperature and maintain the structures of the coils, the current density of the S-bend was calculated to be 8.356 A/mm^2.

5.6.1 water flow rate

In a water-cooling system, heat is removed by water in the conductor cavity, this means that every liter of water per second draws 4.186 kilowatt when the water temperature increases by 1℃.

Then, the heat load $\dot{Q}$ is:

$$\dot{m} = \frac{\dot{Q}}{C_p \cdot \Delta T} \quad \text{..... (49)}$$

Where $\dot{m}$ is the mass flow rate of water (kg/s) $\dot{Q}$ is the heat load in (W), C_p = Specific heat capacity of water (approximately 4180 J/kg·K), and ΔT is a change in temperature from 40 ºC to 45 ºC in this situation.

Assume $\dot{Q}$= 332.31W, then the mass flow rate:

$$\dot{m} = \frac{332.31}{4180 \times 5} = 0.0159 \text{ kg /s} \quad \text{..... (50)}$$

Convert the mass flow rate to volumetric flow rate using the density of water at 40°C (approximately 992 kg/m³):

$$Q = \frac{\dot{m}}{\rho} = \frac{0.0159}{992} = 1.6 \times 10^{-5} m^3 / s \quad \text{..... (51)}$$

Then, convert to litter per minute:

$$Q = 1.6 \times 10^{-5} m\frac{3}{s} \times 60 = 0 \cdot 96 L / min \quad \text{..... (52)}$$

5.6.2 The average velocity

The velocity of the cooling water should respect a given limit to guarantee a turbulent flow, the average velocity is:

$$v_{avg} = \frac{Q}{\pi r^2} \quad \ldots\ldots\ldots\ldots\ldots\ldots \quad (53)$$

where r the radius of the cooling pipe (1.5mm), and Q is the water flow rate in m^3 / s.

$$v_{avg} = \frac{1.6\times10^{-5}}{\pi\cdot(1.5\times10^{-3})^2} \quad \ldots\ldots\ldots\ldots\ldots\ldots \quad (54)$$

$$v_{avg} = \frac{1.6\times10^{-5}}{\pi(2.25\times10^{-6})} = 2.26\, m/s$$

For efficient cooling, the velocity of water should be greater than:

$$v > \frac{1.4}{d} = 0.46 \quad \ldots\ldots\ldots\ldots\ldots\ldots \quad (55)$$

$$v > 0.46 \quad \ldots\ldots\ldots\ldots\ldots\ldots \quad (56)$$

It is worth mentioning that increasing the speed of the water flow more than this will lead to corrosion of the cooling tube.

5.6.3 Reynolds number

Reynolds number is a dimensionless factor and is used to determine the flow regime (laminar, turbulent, or transitional), Turbulent water flow is achieved if $R_e > 4000$, laminar if $R_e < 2000$, and transition if $2000 < R_e < 4000$. Reynolds number represents the ratio between the inertial forces and viscous forces:

$$R_e = \frac{v_{avg}\cdot d}{V} \quad \ldots\ldots\ldots\ldots\ldots\ldots \quad (57)$$

where v is the water velocity, V is the kinematic viscosity of water (0.7×10^{-6} m^2/s at 40℃), and d is the diameter of the cooling pipe, so that:

$$R_e = \frac{2.26\times0.003}{0.7\times10^{-6}} = 9685.7 \quad \ldots\ldots\ldots\ldots\ldots\ldots \quad (58)$$

So, the Reynolds number is 9685.7 which means the flow is turbulent, this facilitates heat transfer efficiency.

5.6.4 Water pressure drop

It is provided by modern cooling systems with maximum pressure up to 2 MPa. lower pressure reduction can be compensated for by an increased cooling flow rate and a more involved coil structure with multiple cooling circuits operating in parallel, the pressure drop is given by the Darcy–Weisbach equation [46]:

$$\Delta p = f \frac{L}{D} \frac{\rho v^2}{2} \quad \ldots\ldots\ldots\ldots\ldots\ldots \quad (59)$$

Where L is the pipe length, ρ is a water density (1000 kg/m^3), and f is the friction factor representing the resistance between the water and the wall of the pipe determined by this equation:

$$f = 0 \cdot 3164 R_e^{-0.25} = 0.032$$

$$\Delta p = 0.032 \frac{16497 \times 10^{-3}}{3 \times 10^{-3}} \frac{1000(2.26)^2}{2} = 449387.1\ Pa = 4.49\ bar \ldots\ldots\ldots\ldots\ldots\ldots \quad (60)$$

Table B.1 (see appendix B) shows the main parameters of the coil for cooling calculations which was used in this research.

5.7 Cost

1. Production-specific Tooling: The estimated cost for tooling the magnet ranges from 5000 € to 15000 €.

2. Yoke: The yoke cost consists of material and manufacturing expenses. Material of Low Carbon Steel costs from 1 € to 1.5 € for each kilogram, and manufacturing cost for the material ranges between 6 € to 10 € for each kilogram. The S- bend magnet estimated mass is 330 – 350 Kilogram.

3. Coil: Coil costs include material and manufacturing expenses. Copper is the chosen material and costs from 10 € to 15 € for each kilogram with an approximate total mass of 15 – 20 Kilogram. The manufacturing costs range from 30 € to 50 € for each kilogram.

Table 10 shows the costs for all of parts for the S- bend dipole magnet.

Table 10

The costs of the S- bend magnet

Item		Cost indication (₵)		Approximate (Kg)		Cost Estimation S-bend (₵)	
		from	to	from	to	from	to
Production-Specific tooling		5000	15000	-		5000	15000
Yoke	Steel / Kg	1	1.5	330	335	330	502.5
	Yoke manufacture	6	10			1980	3350
Coil	Copper conductors	10	15	15	20	150	300
	Coil manufacture	30	50			300	500
Total		Steel sheets				7760	19652.5

Chapter Six

Discussions and Conclusions

This thesis comes in two parts. In the first part: the undulator radiation of the U20 was studied for potential installation SESAME. In the second part, a magnetic design for sector dipole for PERLE was carried out.

The purpose of this study was to characterize the spectral performance of the U20 undulator of 20 mm period length installed in synchrotron facilities such as SOLEIL, specifically the photon flux and brightness, under different beam parameters at SESAME, and to evaluate its quality before any construction step. Understanding the behavior of the U20 undulator with SESAME's parameters is essential before installation, with all radiation characteristics must be quantified and optimized in advance.

Brightness is the main parameter that measures the intensity of synchrotron radiation, which is important in many experiments in different fields of medicine, chemistry, and biology. Therefore, in this thesis, we studied the brightness and the photon flux as a function of energy under the influence of the emittance and energy spread in two cases of the zero emittance and zero energy spread, which is called the ideal case, and the case of non-zero emittance and non-zero energy spread.

From the ideal case, it is noted that only odd harmonics appear due to the on-axis emission, while the even harmonics are suppressed due to the planar undulator symmetry. In this case, the photon flux and brightness are very high.

The analysis began by computing the radiation spectrum for harmonics H1, H2, H10, and H11, using SESAME's emittance of 26 nm.rad and the measured energy spread of 0.1703%. At this case, the peak flux values were found to be approximately 2.46×10^{13} for H1, 3.83×10^{12} for H2, 1×10^{12} for H10, and 5.27×10^{11} for H11. The brightness values reached the order of 10^{19} for the first harmonic, and 10^{17} – 10^{18} for the high harmonics.

To evaluate the impact of beam quality on the undulator performance, when the emittance reduced to 0.26 nm.rad, while keeping the energy spread constant, the flux and brightness significantly increased for all harmonics. For example, the brightness of H1 increased

from 10^{19} to 10^{20}. while higher harmonics such as H10 and H11 also show enhancement due to the reduced source size and angular divergence. These results clearly indicate how a future upgrade of SESAME toward lower emittance would improve its photon output, especially in soft and hard X-ray applications.

The other part in this thesis was about magnet system for the PERLE accelerator in Orsay, France. A future accelerator for the science [47]. PERLE is a three turn ERL and it consists from a LINAC that contains a RF cavity, 6 arcs that contains an S-dipole magnets to bend the electron beam by 30º. The dipole magnet was modeled and analyzed using the Opera-3D simulation package at IJCLab. Opera 3D simulation helps to create the dipole and use its magnetostatic analysis to find the values of the magnetic field around the dipole.

A dipole magnet was designed with a current of 252.74 A, an energy gap of 40 mm, and 91 turns of the coil to achieve the required magnetic field of 1.342 T, with 63.75 cm radius of curvature, and sagitta of 2.17 cm, a 0.72 mm $x_{optimized}$ which is point along x-axis that the field is homogeneity and its be inside in the good field region of the dipole, which was designed for the PERLE accelerator as part of this research. A water-cooling system is used in the field of normal-conducting magnets. This is essential to maintain thermal stability and prevent coil increase in heat, with a calculated Reynolds number of 9685, which is above 4000, meaning the flow is turbulent.

In light of the work presented in this thesis, the focus was on the magnetic system in terms of design, analysis, and optimization, especially the magnets and undulators for the SESAME and PERLE accelerators. An-Najah National University has made concrete scientific and technical contributions to both PERLE and SESAME. Our active participation in the PERLE collaboration, particularly in the design and evaluation of its dipole magnet, and the results of this work will form part of the Technical Design Report (TDR) for PERLE, along with our potential to contribute to SESAME through undulator related studies, demonstrates a national competence in accelerator magnet development and radiation source technologies.

References

[1] Bharti, A., & Goyal, N. (2019). "Fundamentals of synchrotron radiation," in *In Synchrotron radiation: Useful and interesting applications*, IntechOpen.

[2] Zimmermann, F. (2022). "Accelerator technology and beam physics of future colliders," *Frontiers in Physics,* vol. 10.

[3] Liénard, A. (1898). "Champ électrique et magnétique produit par une charge concentrée en un point et animée d'un mouvement quelconque," *L'Éclairage Électrique,* vol. 16, pp. 5-21.

[4] Balerna, A., & Mobilio, S. (2014). "Introduction to synchrotron radiation," in *In Synchrotron radiation: Basics, methods and applications*, Springer Berlin Heidelberg, pp. 3-28.

[5] Bulou, H., Joly, L., Mariot, J.-M., & Scheurer, F. (2021). "Magnetism and accelerator-based light sources," in *In Proceedings of the International School "Synchrotron Radiation and Magnetism"*, Mittelwihr, France, Springer, pp. 1-15.

[6] Mobilio, S., Boscherini, F., & Meneghini, C. (2016). Meneghini, Synchrotron radiation, Springer.

[7] Nadji, A., & The SESAME Project Team. (2010). "Status of the SESAME project," in *In Proceedings of the Particle Accelerator Conference (PAC)*, Vancouver, Canada (WE5RFP022).

[8] Steier, C., & The ALS-U Team. (2019). "Design progress of ALS-U, the soft X-ray diffraction limited upgrade of the Advanced Light Source", In Proceedings of the International Particle Accelerator Conference (IPAC) (TUPGW097).

[9] Kempson, V., & The Diamond Light Source Team. (2006). "Commissioning of the booster synchrotron for the Diamond Light Source," in *In Proceedings of the Particle Accelerator Conference (PAC)*.

[10] Stant, L., & The Diamond-II Team. (2022). "Diamond-II electron beam position monitor development," in *In Proceedings of the International Particle Accelerator Conference (IPAC)*.

[11] Ropert, A., & Farvacque, L. (2006). "Optimization of a new lattice for the ESRF storage ring," in *In Proceedings of the European Particle Accelerator Conference (EPAC) (WEPCH011).*

[12] Carmignani, N., & The ESRF Team. (2018). "Operation improvements and emittance reduction of the ESRF booster," in *In Proceedings of the International Particle Accelerator Conference (IPAC) (THPMF017)*.

[13] Loulergue, A., Blanc-Garcia, O. R., Brunelle, P., Foosang, W., Gamelin, A., Nadji, A., Nadolski, L. S., Nagaoka, R., & Tordeux, M.-A. (2018). "Baseline lattice for

the upgrade of SOLEIL (2.75 GeV)," in *In Proceedings of the International Particle Accelerator Conference (IPAC) (paper THPML034)*.

[14] Smaluk, V., & Shaftan, T. (2019). "Realizing low-emittance lattice solutions with complex bends," *Journal of Physics: Conference Series,* vol. 1350, p. 012044.

[15] Takao, M. (2013)."Beam dynamics and collective effects in “ultimate” storage rings," in *In Proceedings of the Particle Accelerator Conference (PAC) (FRXAA01)*.

[16] Tigner, M. (1965). "A possible apparatus for electron clashing-beam experiments," *Il Nuovo Cimento,* vol. 37, no. 3, pp. 1228-1231.

[17] Tigner, M. (1965). "10 years of ALICE: From concept to operational user facility," in *In Proceedings of the Advanced Beam Dynamics Workshop on Energy Recovery Linacs (ERL), Stony Brook*, NY, USA.

[18] Neil, G. R., et al. (2000). "Sustained kilowatt lasing in a free-electron laser with same-cell energy recovery," *Physical Review Letters,* vol. 84, no. 5, pp. 662-665.

[19] Benson, G. S. V., et al. (2012). "A synchronized FIR/VUV light source at Jefferson Lab," in *In V. Suller (Ed.), Proceedings of the International Particle Accelerator Conference (IPAC)*.

[20] Pietralla, N. (2018). "Laboratory portrait: The Institute of Nuclear Physics at the TU Darmstadt," *Nuclear Physics News,* vol. 28, no. 2, pp. 4-11.

[21] Hoffstaetter, G. H., et al. (2017). "CBETA design report: Cornell-BNL ERL test accelerator (arXiv:1706.04245)," Cornell University.

[22] Schlimme, B. S., et al. (2021). "Operation and characterization of a windowless gas jet target in high-intensity electron beams," *Nuclear Instruments and Methods in Physics Research Section A: Accelerators, Spectrometers, Detectors and Associated Equipment,* vol. 1013, p. 165668.

[23] Agostini, P., et al. (2021). "The Large Hadron-Electron Collider at the HL-LHC," *Journal of Physics G: Nuclear and Particle Physics,* vol. 48, no. 11, p. 110501.

[24] Angal-Kalinin, D., Arduini, G., Auchmann, B., Bernauer, J., Bogacz, A., Bordry, F., … & Zomer, F. (2018). "PERLE: Powerful energy recovery linac for experiments—Conceptual design report," *Journal of Physics G: Nuclear and Particle Physics,* vol. 45, no. 6, p. 065003.

[25] Gutfleisch, O., Willard, M. A., Brück, E., Chen, C. H., Sankar, S. G., & Liu, J. P. (2011)."Magnetic materials and devices for the 21st century: Stronger, lighter, and more energy efficient," *Advanced Materials,* vol. 23, no. 7, pp. 821-842.

[26] Russenschuck, S., & Gupta, R. (2017). "Design and analysis of superconducting accelerator magnets," *IEEE Transactions on Applied Superconductivity,* vol. 27, no.

4, p. 4000509.

[27] Zickler, T. (2011). "Basic design and engineering of normal-conducting, iron-dominated electromagnets," *arXiv preprint arXiv,* vol. 1103, p. 1119.

[28] Ginzburg, V. L. (1947). "Radiation from uniformly moving electrons," *Journal of Physics (USSR),* vol. 10, no. 7, p. 355–362.

[29] Motz, J. W. (1951). "Applications of the radiation from fast electrons," *Journal of Applied Physics,* vol. 22, no. 5, pp. 527-535.

[30] Halbach, K. (1981). "Physical and optical properties of rare earth cobalt magnets," *Nuclear Instruments and Methods in Physics Research,* vol. 187, no. 1, pp. 109-117.

[31] Turner, S. (1998). "Synchrotron radiation and free-electron lasers," in *In CERN Accelerator School: Proceedings*.

[32] Helliwell, J. R. (2017). "New developments in crystallography: Exploring its technology, methods, and scope in the molecular biosciences," *Bioscience Reports,* vol. 37, no. 4, p. BSR20170204.

[33] U.S. Department of Energy, Office of Science, Basic Energy Sciences. (n.d.). *Experimental techniques at light-source beamlines.* Retrieved from https://science.osti.gov/-/media/bes/pdf/Synchrotron_Techniques.pdf.

[34] Chubar, O., & Elleaume, P. (1998). "Accurate and efficient computation of synchrotron radiation in the near field region," in *In Proc. European Particle Accelerator Conference*, Stockholm.

[35] Chubar, O., & Elleaume, P. (2004). "SOLEIL insertion devices: The progress report," in *In Proceedings of the European Particle Accelerator Conference (Paper MOPKF031)*, CERN.

[36] Benabderrahmane, C., Béchu, N., Berteaud, P., Chapuis, L., Couprie, M. E., Daguerre, J. P., … & Zerbib, D. (2011). "Development of $Pr_2Fe_{14}B$ cryogenic undulator CPMU at SOLEIL," in *In Proceedings of the International Particle Accelerator Conference (IPAC),* https://accelconf.web.cern.ch/IPAC2011/papers/thpc149.pdf.

[37] Kim, K.-J. (1986). "Brightness, coherence and propagation characteristics of synchrotron radiation," *Nuclear Instruments and Methods in Physics Research Section A: Accelerators, Spectrometers, Detectors and Associated Equipment,* vol. 246, no. 1-3, pp. 71-76, https://doi.org/10.1016/0168-9002(86)90048-3.

[38] Ghaith, A. (2019). *Towards compact and advanced free electron laser,* Université Paris-Saclay, https://tel.archives-ouvertes.fr/tel-02375533.

[39] Fowles, G. R. (1989). Introduction to modern optics, 2nd ed., Dover Publications.

[40] Rays, G., & Light, V. (n.d). "The Electromagnetic Spectrum," *Aviation,* vol. 118, p. 137.

[41] Abbadi A et al. (2022). J. Phys.: Conf. Series 2380 012036.

[42] SESAME, (2022). "XAFS beamline: Technical design report and user operation manual," SESAME Documentation Series, SESAME Light Source, Jordan.

[43] Klein, M., Hutton, A., Angal-Kalinin, D., Aulenbacher, K., Bogacz, A., Hoffstaetter, G., … & Zimmermann, F. (2022). "Energy-recovery linacs," *CERN Yellow Reports: Monographs,* vol. 1, p. 185, https://doi.org/10.23731/CYRM-2022-001.

[44] 3DS SIMULIA Dassault Systèmes. (2022). *Opera (version 2022 SP2).* Dassault Systèmes. https://www.3ds.com/products-services/simulia/products/opera/

[45] Tanabe, J. T. (2005). Iron-dominated electromagnets: Design, fabrication, assembly, and measurements, World Scientific.

[46] Çengel, Y. A., & Cimbala, J. M. (2018). Fluid mechanics: Fundamentals and applications, 4th ed., McGraw-Hill Education.

[47] PERLE Collaboration. (2017). *PERLE: A High Power Energy Recovery Linac (ERL) – Conceptual Design Report*. arXiv:1705.08783. https://arxiv.org/pdf/1705.08783.pdf

Appendices

Appendix A

Figures

Figure A.1

Schematics

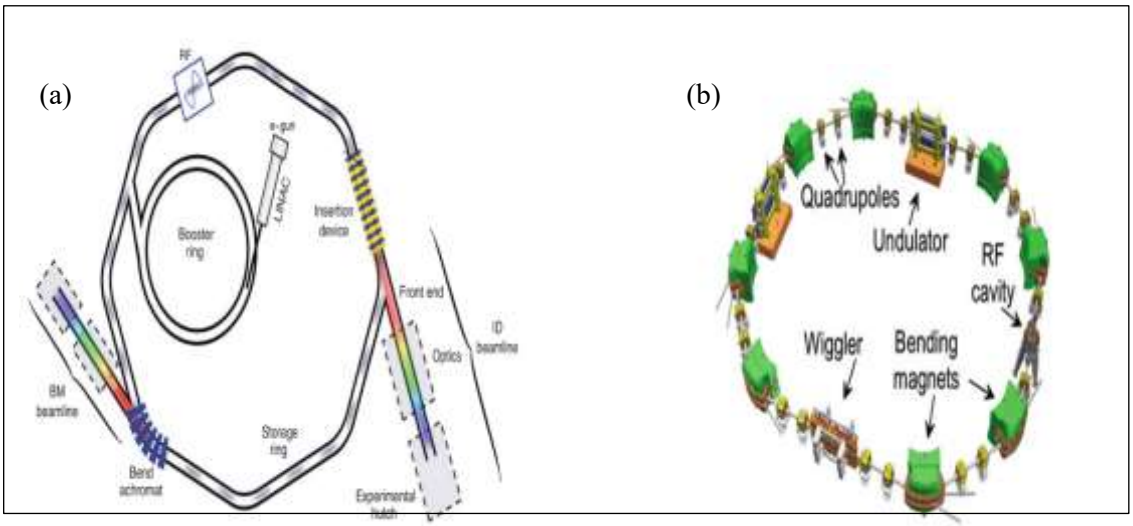

Note: (a) Schematic view of the synchrotron [5]. (b) Schematic view of the storage ring [6]..

Figure A.2

Electron energy in MeV vs electron current in mA of the all ERL

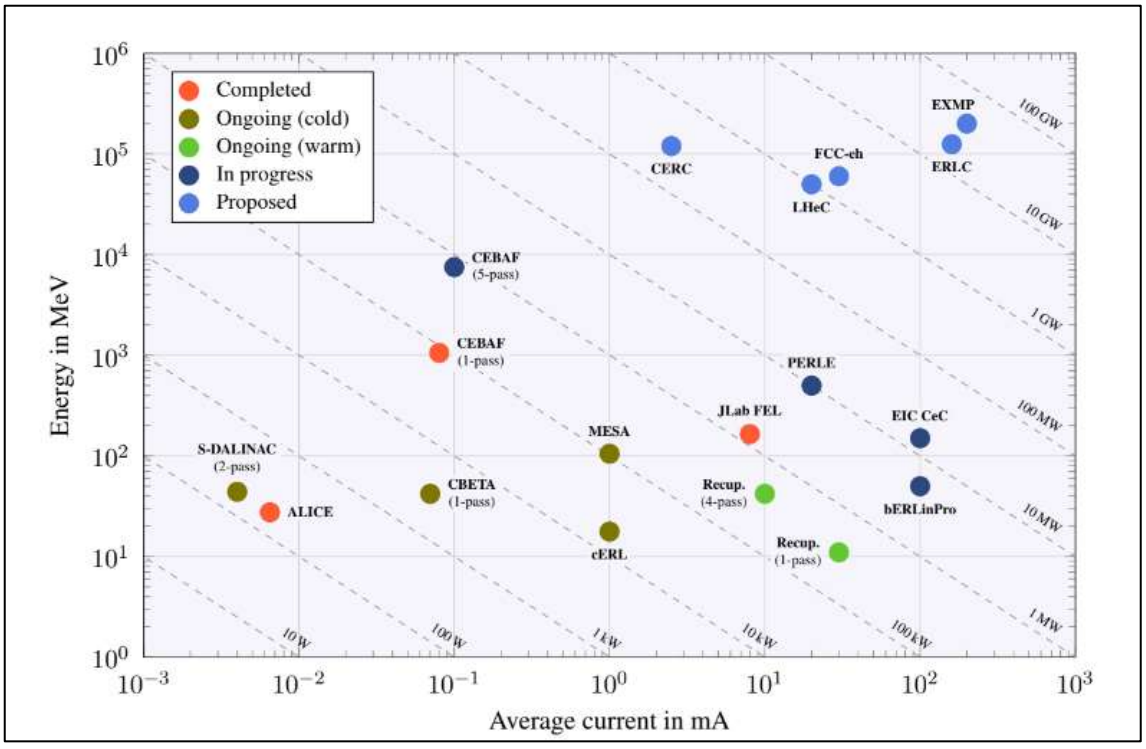

Figure A.3

PERLE top view footprint of 500 MeV

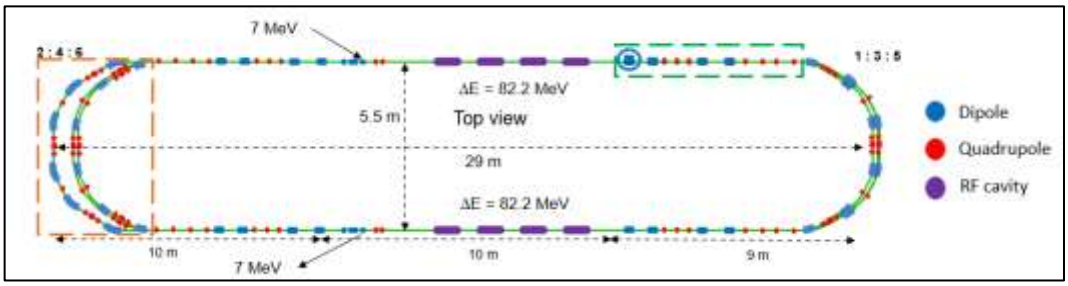

Figure A.4

Right-handed coordinate system used for describing the dipole magnetic field and beam dynamics

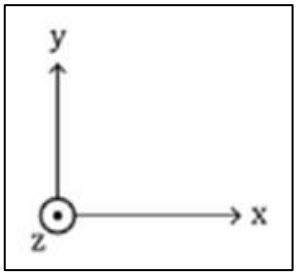

Figure A.5

Schematic of electromagnetic dipoles

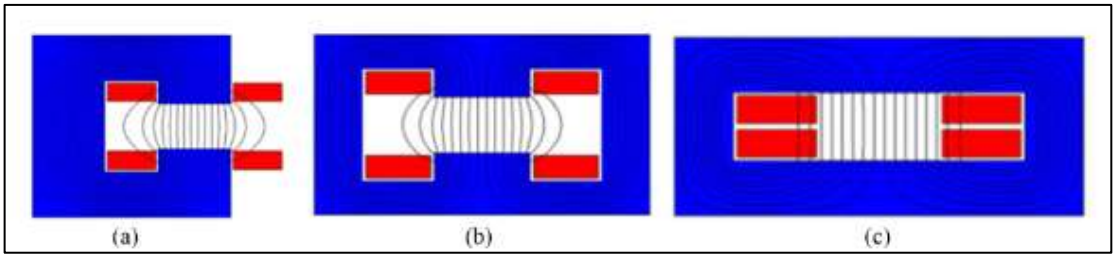

Note: (a) C-shaped. (b) H-shaped. (c) O-shaped. The blue part represents the yoke, while the red part represents the coil.

Figure A.6

Schematic view of the H- Shaped magnetic force (F) acting on a negatively charged particles travelling into the page through on dipole magnet

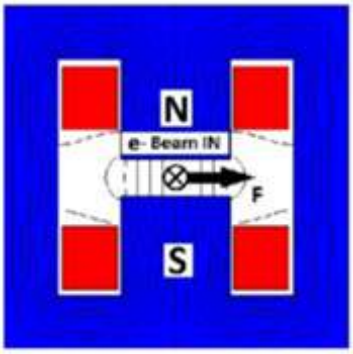

Figure A.7

Ideal pole profile for the dipole

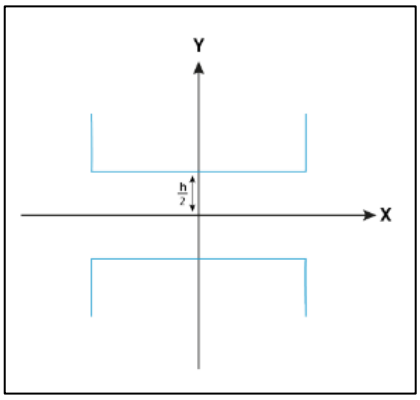

Figure A.8

Schematic view illustrated for the dipole shows paths to finding the excitation current

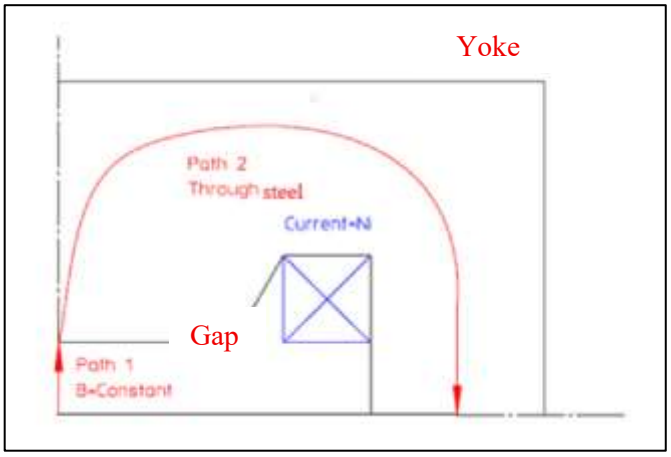

Figure A.9

Schematic representation of a Halbach-based undulator

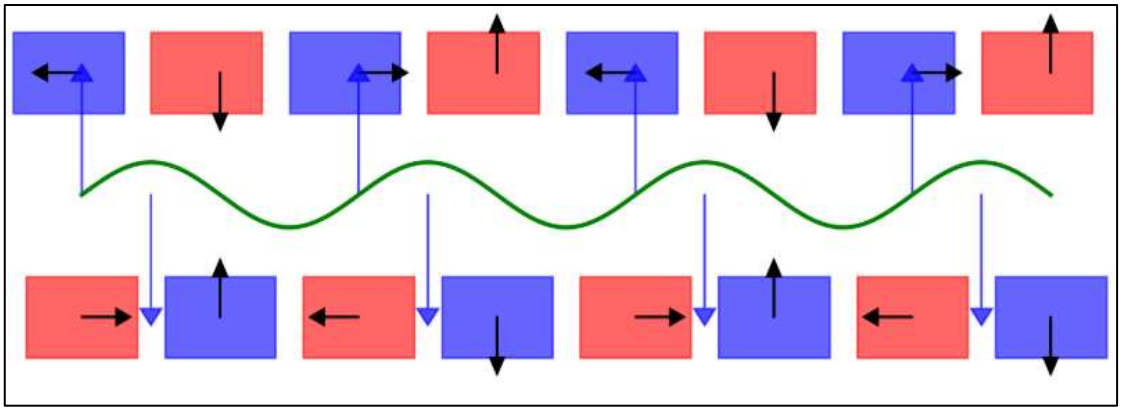

The red and blue blocks correspond to permanent magnets arranged in a Halbach sequence, the black arrows show their magnetization directions, the green sinusoidal line represents the oscillating electron trajectory, and the blue arrows illustrate the concentrated magnetic flux in the beam region.

Figure A.10

Schematic view for general ID

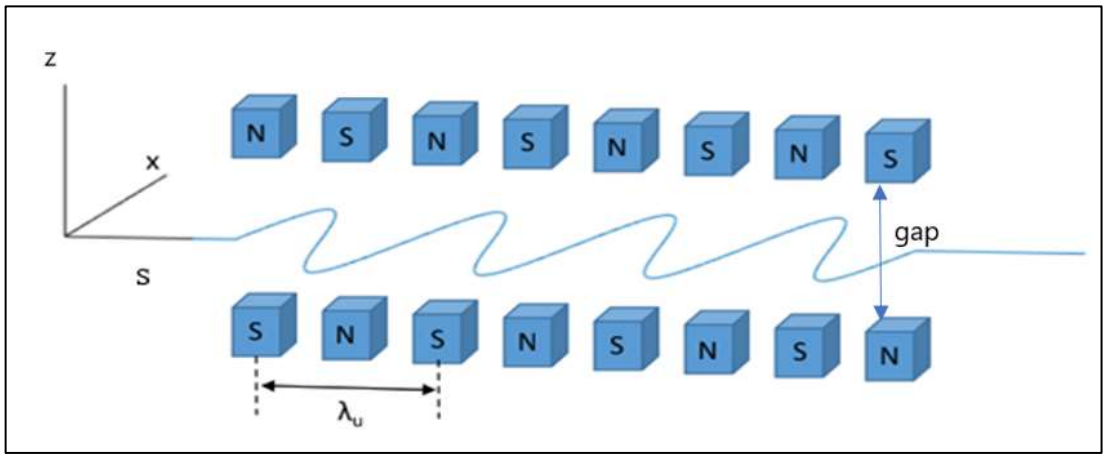

Figure A.11

Angular distribution of the radiation emitted by the undulator

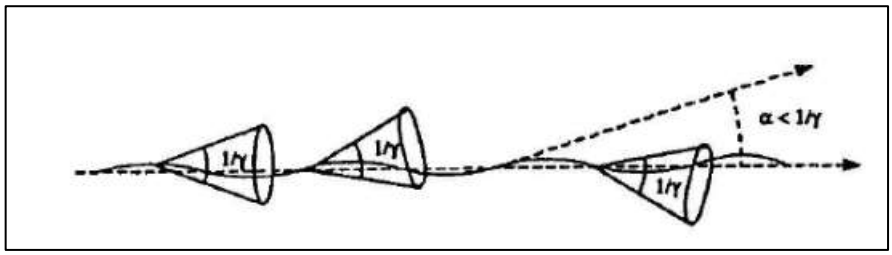

Figure A.12

Schematic review of the coordinate system

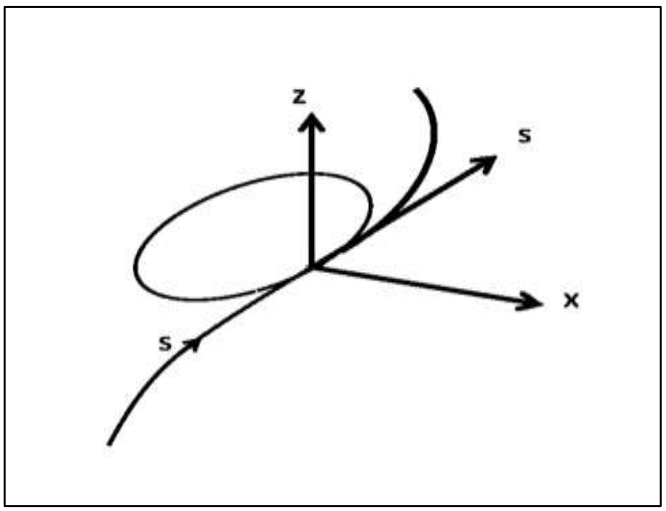

Figure A.13

Interference of undulator radiation

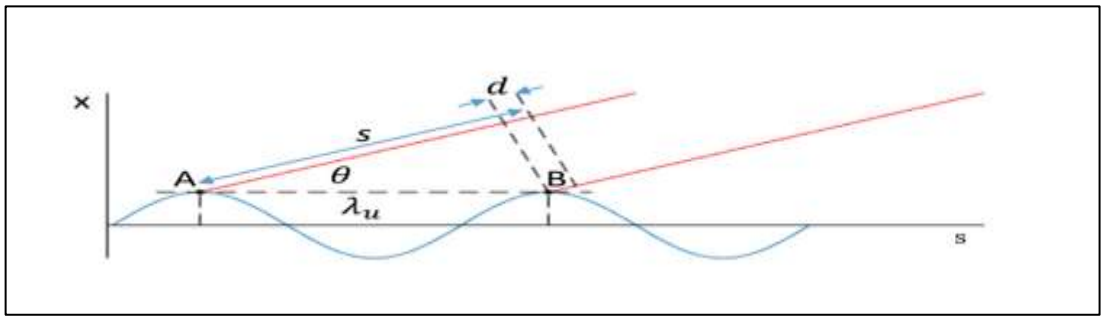

Figure A.14

Schematic view of the energy oscillates about the synchronous orbit

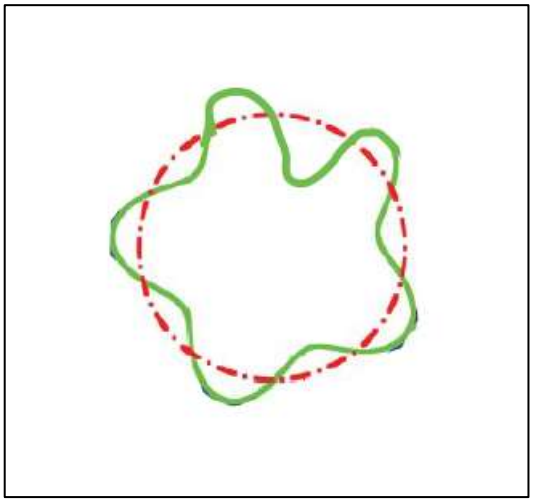

Figure A.15

Schematic view of Gaussian distributions of the electron beam energy around the nominal energy $E_{nominal}$

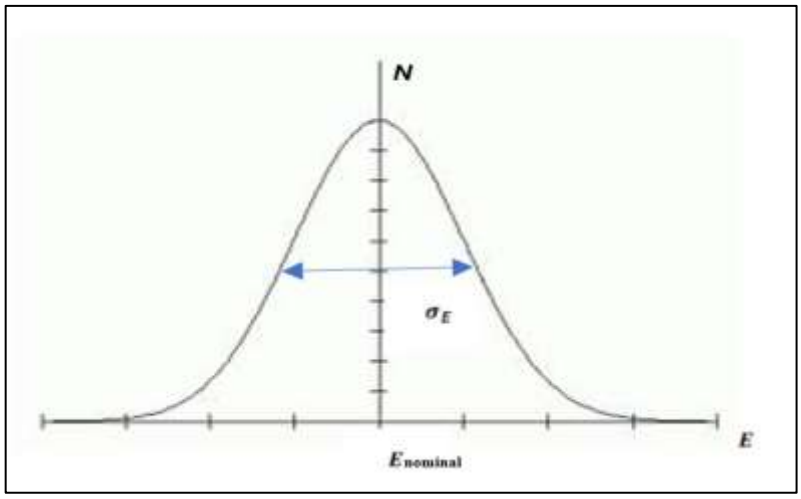

Figure A.16

Photograph of the in-vacuum U20 undulator at Synchrotron SOLEIL

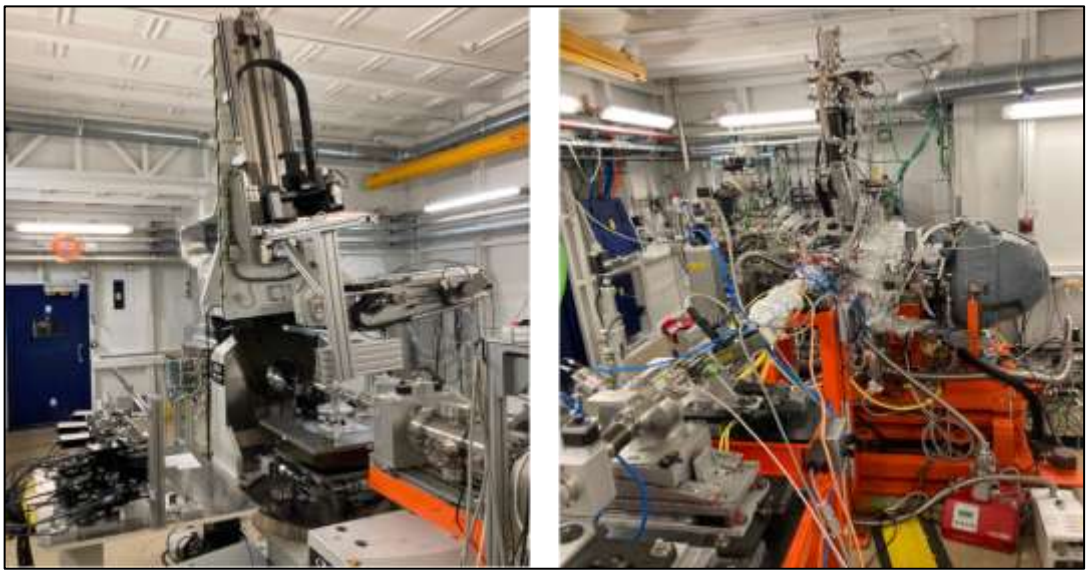

Figure A.17

The explanatory figure for the working process of accelerating the electron beam of PERLE

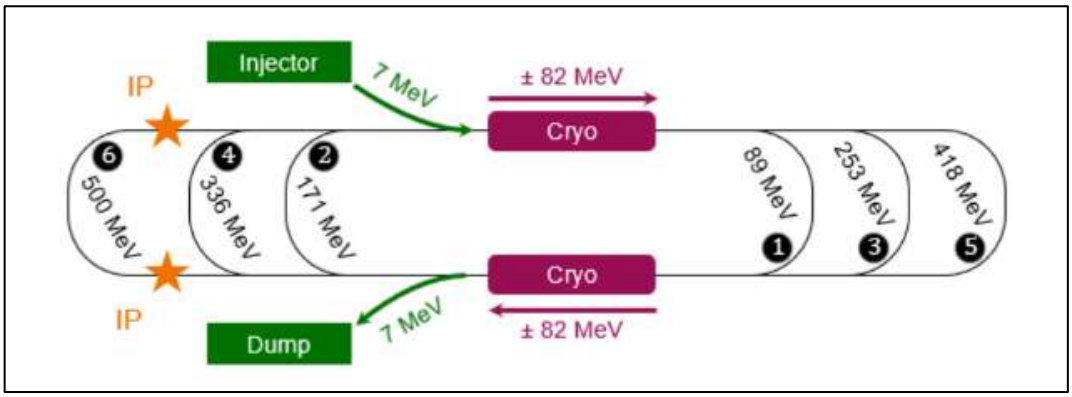

Figure A.18

Dipoles and quadrupoles of spreader/ combiner and arcs sections with blue color of dipoles and red color of quadrupole

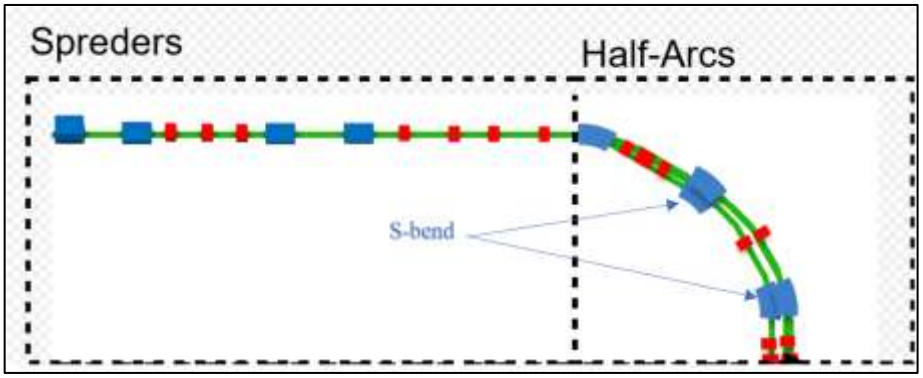

Figure A.19

The spreader/ combiner section with S- bend magnet

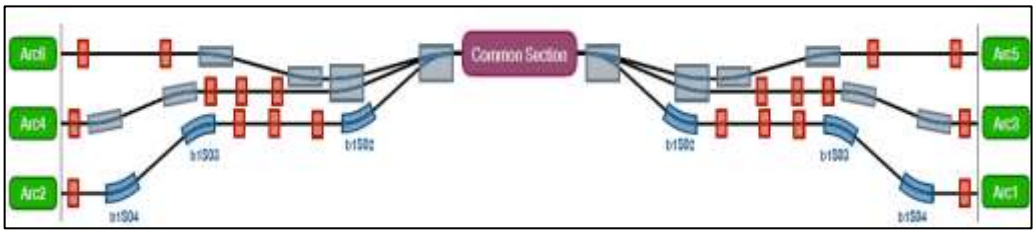

Figure A.20

Side view of the S- bend magnets in arcs of PERLE

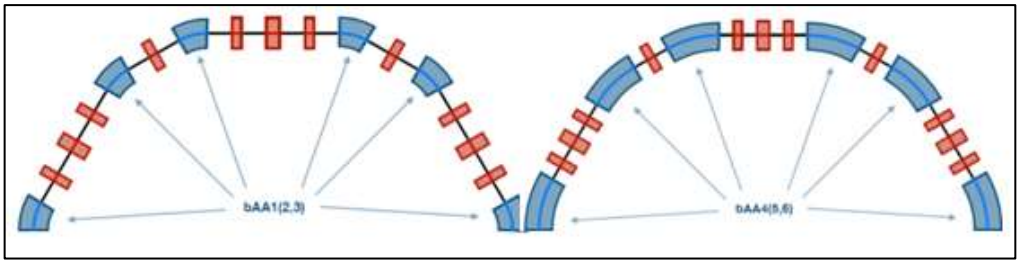

Figure A.21

The blue parts represent dipole magnets and the red parts represent quadrupole magnets

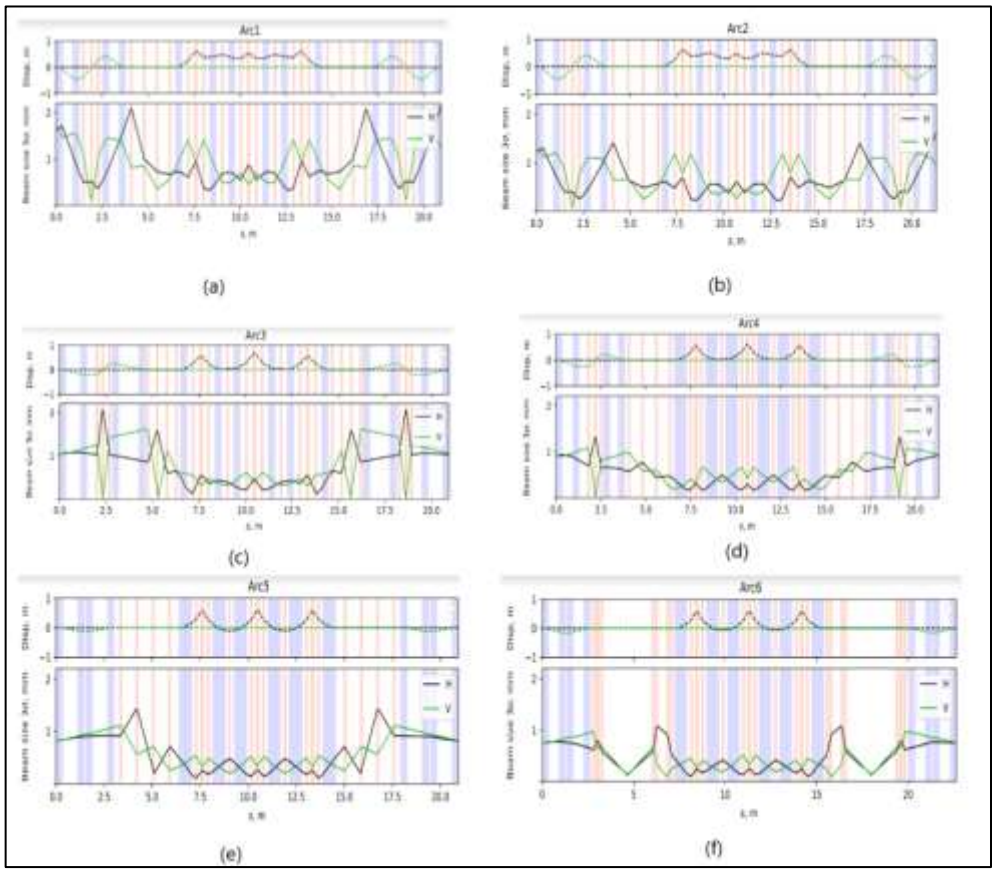

Figure A.22

3D design of the S- bend dipole with Opera

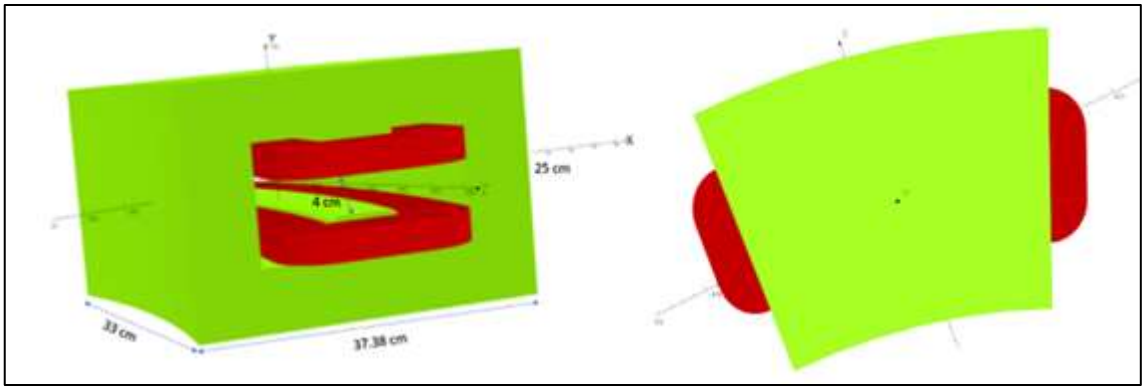

Appendix B

Tables

Table B.1

Cooling calculations of the coil

Variables	Values
Magnetic field (T)	1.342
Diameter (mm)	3
Conductor	5×5
I (A)	252.7472527
J (A/mm^2)	8.356
Number of turns	91
NI Coil (AT)	23000
Number of pancakes	7
One turn length	1269
Coil turns (m×n)	13 / 7
Layer length (mm)	16497
Pancake length (mm)	16497
Copper length (mm)	115479
Copper volume	2.06130015
Copper mass (kg)	18.34557134
Estimation range cost (€)	183.4557 /275.18357
Average Estimation cost (€)	229.3196417
Coil resistance (Ω)	0.10998
Resistance per pancake	0.015711429
Flow rate per pancake Q (L/min)	0.955870951
Coil flow	6.691096658
Pressure for one pancake (bars)	4.49
Speed in a pancake (m/s)	2.253913977
Reynolds number (water 45˚C)	9685.7
Fluid dynamics	Turbulent
	accepted

جامعة النجاح الوطنية
كلية الدراسات العليا

تأثير انبعاث الحزمة على تدفق الفوتون وسطوع اشعاع السنكروترون المنبعث من المموج U20

إعداد
ذياب عبد الحكيم دياب دبيك

إشراف
د. هديل أبو الرب
أ. د. سمير خضير

قدمت هذه الرسالة استكمالا لمتطلبات الحصول على درجة الماجستير في الفيزياء، من كلية الدراسات العليا، في جامعة النجاح الوطنية، نابلس – فلسطين.

2026

تأثير انبعاث الحزمة على تدفق الفوتون وسطوع اشعاع السنكروترون المنبعث من المموج U20

إعداد

ذياب عبد الحكيم دياب دبيك

إشراف

د. هديل أبو الرب

أ. د. سمير خضير

الملخص

تتناول هذه الأطروحة الأداء الإشعاعي للمُموج U20 تمهيداً لتركيبه مستقبلًا في SESAME synchrotron، بالإضافة إلى التصميم المغناطيسي لمغناطيس ثنائي القطب لمسارع PERLE. تهدف الدراسة إلى تقييم تأثير خصائص حزمة الالكترونات على تدفق الفوتونات وسطوعها، وتقديم نموذج مغناطيسي دقيق لمسارع PERLE.

باستخدام برنامج محاكاة SRW، تم تحليل المُموج U20 بوجود حزمة SESAME الواقعية، مما ظهر أن تقليل الانبعاثية الأفقية يُحسِّن ناتج الضوء بشكل كبير: فقد ارتفع التوافقي الأساسي من 2.46×10^{13} إلى 3.28×10^{13}، بينما تحسَّن السطوع بما يقارب عشرة أضعاف. وبالتالي يُمكن لـ SESAME الاستفادة مباشرة من هذه التحسينات في الأداء عند إجراء التحديثات المستقبلية.

في الجزء الثاني، تم تصميم مغناطيس ثنائي القطب لمسارع PERLE وتحسينه باستخدام برنامج Opera 3D، مما حقق جودة مجال مُنتظمة عبر منطقة المجال الجيد، وأكد كفاءة نظام التبريد المائي المضطرب ($Re = 9685.7$). يشكل النموذج المغناطيسي الناتج جزءًا من تقرير التصميم الفني لمشروع بيرل (PERLE). وبشكل عام، تساهم نتائج هذا العمل في تحسين أداء جهاز التموج في مركز SESAME وفي تطوير المغناطيسات لمشروع بيرل.

الكلمات المفتاحية: إشعاع الأنديوليتر، تدفق الفوتونات، السطوع، مغناطيس ثنائي القطب، إشعاع السنكروترون، المسرع الخطي لاستعادة الطاقة.